Transient dynamic robust topology optimization methodology for continuum structure under stochastic uncertainties

Zeng Meng[a, b*], Zixuan Tian[a], Yongxin Gao[a], Matthias G.R. Faes[c], Quhao Li[d*]

[a]*School of Civil Engineering, Hefei University of Technology, Hefei 230009, PR China*

[b]*Jianghuai Advance Technology Center, Hefei 230000, PR China*

[c]*TU Dortmund University, Chair for Reliability Engineering, Leonard-Euler-Straße 5, 44227 Dortmund, Germany*

[d]*Key Laboratory of High Efficiency and Clean Mechanical Manufacture of MOE, School of Mechanical Engineering, Shandong University, Jinan 250061, PR China*

Abstract

Time-variant uncertainties are omnipresent in engineering systems. These significantly impact the structural performance. The main challenge in this context is how to handle them in dynamic domain response topology optimization. To tackle this challenge, a new transient dynamic robust topology optimization (TDRTO) method is proposed to optimize the topology of continuous structures. This method comprehensively considers the uncertainties of material property, loading directions, and time-variant stochastic parameters of loading amplitudes. The time-variant performance function is transformed into a set of independent instantaneous performance functions, where the stochastic processes are discretized by using the optimal linear estimation method to simulate the correlations among various time nodes. The mean and standard deviation of the structural compliance are approximated through a Taylor expansion. Moreover, the Hilber-Hughes-Taylor α method is employed to address the structural dynamic problem. The design and stochastic sensitivities are derived by the "discretize-then-differentiate" and the adjoint methods, thereby improving the computational efficiency. Three illustrative cases are tested to validate the efficacy of TDRTO method, which shows its superiority over the traditional robust topology optimization method for dealing with time-variant stochastic uncertainties.

Keywords: Robust topology optimization; Transient response; Time-variant robust analysis; Uncertainty; Dynamic compliance

*Corresponding author, Email address: mengz@hfut.edu.cn (Z. Meng). quhaoli@sdu.edu.cn (Q. Li).

1. Introduction

Topology optimization (TO) techniques have evolved significantly since the late 1980s [1, 2]. The advent of dynamic TO [3] has greatly fueled this advancement, which offers an indispensable tool in structural design. The widely used static TO methods focus on finding optimized designs under static loading conditions. However, it becomes imperative to consider the time-variant characteristics and inertial effects of engineering structures when dealing with high-frequency excitations [4, 5]. In such scenarios, dynamic response TO emerges and becomes the popular approach [6-9].

Dynamic response TO is broadly divided into two types: frequency domain optimization method and time domain optimization method. Frequency domain optimization method aims to mitigate structural vibration under harmonic or periodic loading conditions. In 1993, Ma et al. [10] pioneered using the homogenization method to minimize the structural frequency response. Subsequently, Pan and Wang [11] introduced an adaptive genetic algorithm to optimize truss structures subjected to the constraints of fundamental frequency, displacement, and acceleration, thereby effectively reducing the structural weight. Since the frequency-domain dynamic response computation requires a large amount of computational effort, Yoon [12] utilized model reduction techniques to compute dynamic responses and sensitivities efficiently, which include modal superposition, Ritz Vector, and quasi-static Ritz Vector methods. For further reducing the computation time of harmonic response for large-scale TO problems, Liu et al. [13] applied the modal displacement method, the modal acceleration method (MAM), and the full method. In the study of Shang et al. [14], the improved MAM is put forward to address the limitations of traditional MAM, which was applied to perform vibro-acoustic coupling analysis under steady-state stochastic excitation. Moreover, Liu et al. [15] minimized the frequency response of honeycomb composites over a specific frequency range that offers a broad design space to enhance its dynamic performance.

Unlike the frequency domain optimization method, dynamic response TO method focuses on handling the time-variant dynamic behavior. For example, Min et al. [16] firstly explored the dynamic response TO problem in the time domain, thereby minimizing the average dynamic compliance through the homogenization techniques. Since dynamic topology optimization involves time discretization, it results in significant computation and storage

demands. Thus, it is extremely time consuming. To tackle this issue, Kang et al. [17] and Jiang et al. [18] converted dynamic loads into equivalent static load (ESL) sets, which significantly reduces the computational time. Subsequently, Kim and Park [19] extended ESL to solve nonlinear dynamic TO problem. However, it was reported that ESL algorithm has limitation for solving dynamic response TO problems, which may result in the misleading topology layout. Thus, Stolpe [20] put forward an improved ESL method that calculated the gradient of the displacement vector at each time node, but it results in expensive computational cost. To enhance computational efficiency, Zhu and Kang [21] adopted the modal displacement method for calculating the quasi-static response, in which an efficient transient dynamic TO framework was further developed.

It should be noted that the above-mentioned dynamic TO mainly focuses on deterministic scenarios, which neglects the impact of inevitable uncertainties incurred by manufacturing errors, environmental changes, and fatigue wear in practical engineering applications [22-26]. It was reported that these time-variant uncertainties profoundly affect the mechanical performance of structures, especially for dynamic structures with different service periods [27-30]. Therefore, it is necessary to employ robust topology optimization (RTO) to address these uncertainties[31-34]. Rostami et al. [35] proposed a novel robust topology optimization method of continuous structures under material and loading uncertainties, which integrated the evolutionary structural optimization method with the extended finite element method to enhance the computational efficiency with clear and smooth structural boundaries. For RTO under uncertain dynamic excitation, Zhang et al. [36] used a non-probabilistic ellipsoidal convex model to describe the dynamic loads and simplified the RTO model into a single-loop optimization model through a generalized flexibility matrix, thereby avoiding complex non-probabilistic calculation. Cai et al. [37] suggested a parallel RTO method for periodic microstructures, where the uncertainties of probabilistic dynamic loads were considered. Zheng et al. [38] combined the RTO method and the level set approach for designing uniform periodic microstructures under stochastic and interval uncertainties, where a hybrid dimension reduction technique with binary reduction schemes was applied to estimate the objective function effectively.

However, the aforementioned studies mainly focus on considering the impact of uncertain dynamic excitation on the structure, while the effects of time-variant characteristics under actual working conditions are ignored [39, 40]. This may result in the misleading results for

assessing performance. Thus, how to put forward the time-variant RTO method is crucial. However, to the best of the author's knowledge, the exploration of RTO with time-variant uncertainties is very scarce. Moreover, the time-variant RTO requires deriving the design and stochastic sensitivities, which also is a challenging work.

This study proposes a new transient dynamic robust topology optimization (TDRTO) model for continuous structure, which can reasonably account for the impact of time-variant uncertainties. The TDRTO model comprehensively incorporates the uncertainties of geometric size, material property, loading direction, and time-variant loading amplitude. The "discretize-then-differentiate" approach and the adjoint method are utilized for deriving design and stochastic sensitivities, where the Lagrange equation is constructed twice. The remaining parts of this article are as below. Section 2 introduces the background of transient dynamic deterministic topology optimization (DTO) model and probabilistic method. Section 3 presents the proposed TDRTO model and the sensitivity calculation. Section 4 explains the numerical implementation. Section 5 presents three numerical examples. Conclusions are presented in Section 6.

2. Background

2.1. Problem statement

Topology optimization (TO) of continuum structures aims to determine the optimal material layout in the design domain [41]. The dynamic compliance $f = \frac{1}{N_t}\int_0^{t_{\max}} \mathbf{F}^T\mathbf{u}(t)dt$ within a specified time interval [0, $t_{\max}$] is widely adopted as the objective function in transient topology optimization (TO) [42, 43], which quantifies dynamic stiffness through temporal integration of structural compliance, thereby minimizing energy dissipation under transient or periodic loading conditions. The mathematical representation of this TO problem is given as:

$$\begin{aligned} \min \quad & J = \frac{1}{N_t}\int_0^{t_{\max}} \mathbf{F}^T\mathbf{u}(t)dt \\ \text{s.t.} \quad & \begin{cases} \mathbf{M}\ddot{\mathbf{u}}(t) + \mathbf{C}\dot{\mathbf{u}}(t) + \mathbf{K}\mathbf{u}(t) = \mathbf{F}(t) \\ \mathbf{u}\big|_{t=0} = \mathbf{u}_0 \\ \dot{\mathbf{u}}\big|_{t=0} = \dot{\mathbf{u}}_0 \\ V \le f_v V_0 \\ 0 \le \rho_e \le 1, e = 1,\ldots, Ne \end{cases} \end{aligned} \tag{1}$$

where N_t denotes the number of time nodes. $\mathbf{F}$ denotes the external excitations. ρ_e represents the design variables. Ne represents the element number. $t_{\max}$ represents the maximum loading time. $\mathbf{M}$, $\mathbf{C}$, and $\mathbf{K}$ represent the mass, damping, and stiffness matrixes. $\mathbf{u}$ represents the displacement vector. $\dot{\mathbf{u}}$ and $\ddot{\mathbf{u}}$ represent the velocity and acceleration vectors. $\mathbf{u}_0$ and $\dot{\mathbf{u}}_0$ represent the initial displacement and acceleration. V denotes the material volume with allowable value $f_v V_0$. The stiffness matrix and mass matrix are computed by

$$\mathbf{M} = \sum_{l=1}^{N} \tilde{m}_V(\rho_e)\mathbf{m}_l, \quad \mathbf{K} = \sum_{l=1}^{N} \tilde{m}_E(\rho_e)\mathbf{k}_l \tag{2}$$

$$\mathbf{m}_l = \int_{\Omega_l} \rho_0 \mathbf{N}_l^T \mathbf{N}_l d\mathbf{x}, \quad \mathbf{k}_l = \int_{\Omega_l} \mathbf{B}_l^T \mathbf{D}_0 \mathbf{B}_l d\mathbf{x} \tag{3}$$

where $\mathbf{m}_l$ and $\mathbf{k}_l$ are the *l-th* element mass and stiffness matrices, respectively. $\mathbf{N}_l$ and $\mathbf{B}_l$ are their respective shape functions and strain-displacement matrices. $\mathbf{D}_0$ represents the material constitutive matrix for linear isotropic materials. $\tilde{m}_V$ and $\tilde{m}_E$ define the volume interpolation function and material interpolation function, respectively [44]. Their definitions are as follows:

$$\begin{aligned} \tilde{m}_V(\rho_e) &= \varepsilon + (1-\varepsilon)m_V(\rho_e) \\ \tilde{m}_E(\rho_e) &= \varepsilon + (1-\varepsilon)m_E(\rho_e) \end{aligned} \tag{4}$$

In Eq. (4), an Ersatz parameter ε is used in $\tilde{m}_V$ and $\tilde{m}_E$ to prevent numerical instability when ρ_e approaches zero.

The volume interpolation function is computed using a threshold projection function [45]:

$$m_V(\rho_e) = \frac{\tanh(\bar{\beta}\omega) + \tanh(\bar{\beta}(\rho_e - \omega))}{\tanh(\bar{\beta}\omega) + \tanh(\bar{\beta}(1-\omega))} \tag{5}$$

where ω denotes the threshold density. $\bar{\beta}$ controls the projection aggressiveness. The stiffness interpolation function is selected by the rational approximation of material properties function [44, 46].

$$m_E(\rho_e) = \frac{m_V(\rho_e)}{1 + p_0[1 - m_V(\rho_e)]} \tag{6}$$

where p_0 is the penalization exponent. The proportional damping is employed to calculate the damping matrix $C = \alpha_r M + \beta_r K$, where α_r and β_r are the Rayleigh damping parameters.

2.2. Uncertainty propagation via Taylor series expansion

To integrate the governing uncertainties in the dynamical TO problem, they need to be modelled mathematically. Probability has been shown both theoretically and practically to be a rigorous approach in this context [47-50]. In the context of RTO, there exists the need to compute the mean and variance of the response to measure the robustness of a design. These quantities are given by:

$$\begin{aligned} \mu\left(g\left(\mathbf{x}\right)\right) &= \int_{\Omega} \{g\left(\mathbf{x}\right) f_{\mathbf{x}}\left(\mathbf{x}\right) d\mathbf{x}\} \\ \sigma^2\left(g\left(\mathbf{x}\right)\right) &= \int_{\Omega} \{g^2\left(\mathbf{x}\right) f_{\mathbf{x}}\left(\mathbf{x}\right) d\mathbf{x}\} \end{aligned} \tag{7}$$

where $g\left(\mathbf{x}\right)$ represents the response function. $f_{\mathbf{x}}\left(\mathbf{x}\right)$ denotes the probability density function. $\mu(g)$ and $\sigma^2(g)$ indicate the mean and variance, respectively.

However, the calculation of complex integral formulas is very challenging in the case of dynamical problems due to the implicit nature and high dimensions of the corresponding integral equations. Since we are dealing with an optimization problem over second order response moments, however, it is sufficient to make accurate predictions in the vicinity of the current iteration. Therefore, the Taylor series expansion method is employed in this paper. For the objective func $f = \left(\mathbf{x}, \boldsymbol{\alpha}\right)$tion , the Taylor expansion can be obtained by introducing $\boldsymbol{\delta} = (\delta_1, \ldots \delta_{Nx})^T$ as follow:

$$f(\mathbf{x} + \boldsymbol{\delta}) = f(\mathbf{x}) + \sum_{i=1}^{Nx} \frac{\partial f}{\partial x_i} \delta_i + \cdots \tag{8}$$

where $\mathbf{x}$ are stochastic variables. *Nx* represents the number of $\mathbf{x}$. Assuming $\mathbf{E}[\boldsymbol{\delta}] = \mathbf{0}$ and the structure is linear, the first-order expected value is 0. If these uncertainty factors are

uncorrelated, the first and second statistical moments [51] of f with respect to (w.r.t.) $\mathbf{x}$ become

$$\begin{aligned}\mu(f(\mathbf{x})) &= \sum_{i=1}^{Nx} f(x_i) \\ \sigma^2(f(\mathbf{x})) &= \sum_{i=1}^{Nx} \left(\frac{\partial f}{\partial x_i}\right)^2 \sigma_i^2\end{aligned} \tag{9}$$

where μ and σ denote the mean and standard deviation (SD), respectively.

3. The transient dynamic robust topology optimization method

3.1. Model establishment

Under practical working conditions, the load at each time instant is stochastic [52]. Thus, it is essential to incorporate time-variant characteristics to form a new TDRTO model. To achieve this goal, the expansion optimal linear estimation (EOLE) [53] method is applied to discretize the stochastic process $\tilde{\mathbf{F}}(t)$, where the time-variant dynamic compliance is reformulated as the corresponding instantaneous dynamic compliance, thereby simulating the dependencies between different time instances. The TDRTO model is constructed as follows:

$$\begin{aligned} \min_{\rho_e} \quad & J = \mu\left(c(\boldsymbol{\rho}, \mathbf{x}, \tilde{\mathbf{F}}(t), t)\right) + \beta\sigma\left(c(\boldsymbol{\rho}, \mathbf{x}, \tilde{\mathbf{F}}(t), t\right) \\ \text{s.t.} \quad & \begin{cases} \mathbf{M}\ddot{\mathbf{u}}(t) + \mathbf{C}\dot{\mathbf{u}}(t) + \mathbf{K}\mathbf{u}(t) = \tilde{\mathbf{F}}(t) \\ \mathbf{u}\big|_{t=0} = \mathbf{u}_0 \\ \dot{\mathbf{u}}\big|_{t=0} = \dot{\mathbf{u}}_0 \\ V \le f_v V_0 \\ 0 \le \rho_e \le 1 \end{cases} \end{aligned} \tag{10}$$

where $c(\boldsymbol{\rho}, \mathbf{x}, \tilde{\mathbf{F}}(t), t)$ represents the dynamic compliance. It is determined by

$$c(\boldsymbol{\rho}, \mathbf{x}, \tilde{\mathbf{F}}(t), t) = \tilde{\mathbf{F}}(t)^T \mathbf{u}(\boldsymbol{\rho}, \mathbf{x}, \tilde{\mathbf{F}}(t), t) \tag{11}$$

where $\tilde{\mathbf{F}}(t)$ is a stochastic process with mean value $\mu_{\tilde{F}}(t)$, SD $\sigma_{\tilde{F}}(t)$, and autocorrelation function $\rho_{\tilde{F}}(t_1, t_2)$. The stochastic process $\tilde{\mathbf{F}}(t)$ is represented by EOLE as:

$$\tilde{\mathbf{F}}(t) = \mu_{\tilde{F}}(t) + \sum_{j=1}^{h} \frac{Z_j}{\sqrt{\chi_j}} \boldsymbol{\Phi}_j^T(t) \boldsymbol{\rho}_{\tilde{F}}(t) \tag{12}$$

where h denotes the number of dominated eigenvalues that should be less than N_t. The

eigenvalues and eigenvectors of covariance matrix are denoted by χ and $\mathbf{\Phi}$. $\boldsymbol{\rho}_{\tilde{F}}(t)$ denotes the time-variant covariance vector and can be calculated by $[\sigma_{\tilde{F}}(t)\sigma_{\tilde{F}}(t_1)\rho_{\tilde{F}}(t,t_1),\sigma_{\tilde{F}}(t)\sigma_{\tilde{F}}(t_2)\rho_{\tilde{F}}(t,t_2),\ldots\sigma_{\tilde{F}}(t)\sigma_{\tilde{F}}(t_{N_t})\rho_{\tilde{F}}(t,t_{N_t})]^T$. Z_j represents the *j*-th uncorrelated normal stochastic variable of $\mathbf{Z}=\left(Z_1,...,Z_j,...,Z_h\right)$ with a standard normal distribution. The parameter *h* controls the accuracy of the stochastic process discretization. A higher *h* results in a more accurate representation of the dependence between different instantaneous dynamic compliance values. According to EOLE expansion in Eq. (12), the time-variant dynamic compliance is determined as below:

$$c(\mathbf{x},\tilde{\mathbf{F}}(t),t)\square\{c(\mathbf{x},\mathbf{Z},t),t_e\in[t_0,t_{\max}],k=1,\cdots N_t\} \tag{13}$$

The instantaneous dynamic compliance at t_e depends on the values at previous time nodes. This correlation is explicitly captured by the EOLE method through the inclusion of $\boldsymbol{\rho}_{\tilde{F}}(t)$. Then, the stochastic process $\tilde{\mathbf{F}}(t)$ is converted into the independent stochastic variables $\mathbf{Z}$, and the dynamic compliance $c(\mathbf{x},\tilde{\mathbf{F}}(t),t)$ becomes $c(\mathbf{x},\mathbf{Z},t)$. In this way, the solutions for $\mu(c)$ and $\sigma(c)$ are computed by using the Taylor expansion for Eqs. (9) and (11), which are formulated as follows:

$$\begin{aligned}\mu(c)&=\frac{1}{N_t}\int_0^{t_{\max}}c(\boldsymbol{\rho},\mathbf{x},\mathbf{Z},t)dt\\ \sigma(c)&=\sqrt{\sum_{i=1}^{Nx}\left(\frac{\partial\frac{1}{N_t}\int_0^{t_{\max}}c(\boldsymbol{\rho},\mathbf{x},\mathbf{Z},t)dt}{\partial x_i}\right)^2\sigma_{x_i}^2+\sum_{j=1}^{Nz}\left(\frac{\partial\frac{1}{N_t}\int_0^{t_{\max}}c(\boldsymbol{\rho},\mathbf{x},\mathbf{Z},t)dt}{\partial Z_j}\right)^2\sigma_{Z_j}^2}\end{aligned} \tag{14}$$

where x_i represents stochastic variables. *Nx* and *Nz* represent the number of stochastic variables and independent standard normal stochastic variable, respectively. $\frac{\partial\frac{1}{N_t}\int_0^{t_{\max}}c(\boldsymbol{\rho},\mathbf{x},\mathbf{Z},t)dt}{\partial x_i}$ and $\frac{\partial\frac{1}{N_t}\int_0^{t_{\max}}c(\boldsymbol{\rho},\mathbf{x},\mathbf{Z},t)dt}{\partial Z_j}$ represent the sensitivity w.r.t. time-invariant stochastic variables **x** and time-variant stochastic variables **Z**, which will be derived in section 3.3.

3.2. Hilber-Hughes-Taylor α method

The (Hilber-Hughes-Taylor α) *HHT-α* method is an extension of the Newmark-*β* method

for solving structural dynamic problems [54-56]. It modifies the motion equations by introducing a parameter α, which accounts the numerical lag between the damping, stiffness, and external force vectors. The generalized α method is depicted as follows:

$$\mathbf{M}\ddot{\mathbf{u}}_{i+1-\alpha_m} + \mathbf{C}\dot{\mathbf{u}}_{i+1-\alpha_f} + \mathbf{K}\mathbf{u}_{i+1-\alpha_f} = \mathbf{F}(t_{i+1-\alpha_f}) \tag{15}$$

$$\begin{aligned} \mathbf{u}_{i+1} &= \mathbf{u}_i + \Delta t\dot{\mathbf{u}}_i + \Delta t^2((\frac{1}{2}-\hat{\beta})\ddot{\mathbf{u}}_i + \hat{\beta}\ddot{\mathbf{u}}_{i+1}) \\ \dot{\mathbf{u}}_{i+1} &= \dot{\mathbf{u}}_i + \Delta t((1-\gamma)\ddot{\mathbf{u}}_i + \gamma\ddot{\mathbf{u}}_{i+1}) \end{aligned} \tag{16}$$

where

$$\begin{aligned} \mathbf{u}_{i+1-\alpha_f} &= (1-\alpha_f)\mathbf{u}_{i+1-\alpha_f} + \alpha_f\mathbf{u}_i \\ \dot{\mathbf{u}}_{i+1-\alpha_f} &= (1-\alpha_f)\dot{\mathbf{u}}_{i+1-\alpha_f}\dot{\mathbf{u}}_i + \alpha_f\dot{\mathbf{u}}_i \\ \ddot{\mathbf{u}}_{i+1-\alpha_m} &= (1-\alpha_m)\ddot{\mathbf{u}}_{i+1-\alpha_m}\ddot{\mathbf{u}}_i + \alpha_m\ddot{\mathbf{u}}_i \\ t_{i+1-\alpha_f} &= (1-\alpha_f)t_{i+1-\alpha_f}t_i + \alpha_f t_i \end{aligned} \tag{17}$$

where Δt represents the time step. The update equations of $\mathbf{u}$, $\dot{\mathbf{u}}$, and $\ddot{\mathbf{u}}$ are identical to those used in the Newmark algorithm.

When $\alpha_m = 0$, $\alpha_f = \alpha$, and $\gamma = \frac{1}{2} + \alpha$, it degenerates into the *HHT-α* algorithm.

$$\mathbf{M}\ddot{\mathbf{u}}_{i+1} + (1-\alpha)\mathbf{C}\dot{\mathbf{u}}_{i+1} + \alpha\mathbf{C}\dot{\mathbf{u}}_i + (1-\alpha)\mathbf{K}\mathbf{u}_{i+1} + \alpha\mathbf{K}\mathbf{u}_i = (1-\alpha)\mathbf{F}(t_{i+1}) + \alpha\mathbf{F}(t_i) \tag{18}$$

where $i \in \{0,1,...,N_t - 1\}$. To guarantee the second-order accuracy and unconditional stability of the *HHT-α* method, the following conditions must be satisfied [54].

$$\begin{aligned} &0 \le \alpha \le 1/3 \\ &\hat{\beta}_i = (1+\alpha)^2/4 \\ &\gamma = (1+2\alpha)/2 \end{aligned} \tag{19}$$

To address the dynamic problem, Eq. (18) is computed to obtain $\ddot{\mathbf{u}}_{i+1}$. $\mathbf{u}_{i+1}$ and $\dot{\mathbf{u}}_{i+1}$ are updated for each time step $i = 0,\ldots,N_t - 1$. For time step $i = 0$, $\mathbf{u}_0$ and $\dot{\mathbf{u}}_0$ are used from the initial conditions, and $\ddot{\mathbf{u}}_0$ is computed by solving $\mathbf{M}\ddot{\mathbf{u}}_0 = \mathbf{F}_0 - \mathbf{C}\dot{\mathbf{u}}_0 - \mathbf{K}\mathbf{u}_0$.

3.3. Stochastic sensitivity analysis

In real-word engineering system, the uncertainties mainly include the geometric size, material property, loading amplitude, and loading direction. When the geometric size and material property are considered as stochastic variables, a Lagrange function L_x is generated by introducing an adjoint vector $\boldsymbol{\lambda}_x(t)$. It is formulated as follows:

$$L_x = \frac{1}{N_t}\int_0^{t_{\max}} \tilde{\mathbf{F}}^T \mathbf{u} dt + \int_0^{t_{\max}} \boldsymbol{\lambda}_x{}^T \left[\mathbf{M}\ddot{\mathbf{u}} + \mathbf{C}\dot{\mathbf{u}} + \mathbf{K}\mathbf{u} - \tilde{\mathbf{F}}\right] dt \tag{20}$$

Then, the sensitivity of L_x w.r.t. x_i is as follows:

$$\frac{\partial L_x}{\partial x_i} = \frac{1}{N_t}\int_0^{t_{\max}} \tilde{\mathbf{F}}^T \frac{\partial \mathbf{u}}{\partial x_i} dt + \int_0^{t_{\max}} \boldsymbol{\lambda}_x{}^T \left[\frac{\partial \mathbf{M}}{\partial x_i}\ddot{\mathbf{u}} + \frac{\partial \mathbf{C}}{\partial x_i}\dot{\mathbf{u}} + \frac{\partial \mathbf{K}}{\partial x_i}\mathbf{u}\right] dt + \int_0^{t_{\max}} \boldsymbol{\lambda}_x{}^T \left[\mathbf{M}\frac{\partial \ddot{\mathbf{u}}}{\partial x_i} + \mathbf{C}\frac{\partial \dot{\mathbf{u}}}{\partial x_i} + \mathbf{K}\frac{\partial \mathbf{u}}{\partial x_i}\right] dt \tag{21}$$

Because there is no correlation between the initial conditions and structural properties, the final term in Eq. (21) becomes

$$\begin{aligned}
&\int_0^{t_{\max}} \boldsymbol{\lambda}_x{}^T \left[\mathbf{M}\frac{\partial \ddot{\mathbf{u}}}{\partial x_i} + \mathbf{C}\frac{\partial \dot{\mathbf{u}}}{\partial x_i} + \mathbf{K}\frac{\partial \mathbf{u}}{\partial x_i}\right] dt \\
&= \left(\boldsymbol{\lambda}_x\big|_{t=t_{\max}}\right)^T \mathbf{M}\frac{\partial \dot{\mathbf{u}}}{\partial x_i}\bigg|_{t=t_{\max}} - \left(\dot{\boldsymbol{\lambda}}_x\big|_{t=t_{\max}}\right)^T \mathbf{M}\frac{\partial \mathbf{u}}{\partial x_i}\bigg|_{t=t_{\max}} + \int_0^{t_{\max}} \left(\ddot{\boldsymbol{\lambda}}_x\right)^T \mathbf{M}\frac{\partial \mathbf{u}}{\partial x_i} dt \\
&\quad + \left(\boldsymbol{\lambda}_x\big|_{t=t_{\max}}\right)^T \mathbf{C}\frac{\partial \mathbf{u}}{\partial x_i}\bigg|_{t=t_{\max}} - \int_0^{t_{\max}} \left(\dot{\boldsymbol{\lambda}}_x\right)^T \mathbf{C}\frac{\partial \mathbf{u}}{\partial x_i} dt + \int_0^{t_{\max}} \left(\boldsymbol{\lambda}_x\right)^T \mathbf{K}\frac{\partial \mathbf{u}}{\partial x_i} dt
\end{aligned} \tag{22}$$

Substituting Eq. (22) into Eq. (21), $\frac{\partial L_x}{\partial x_i}$ is calculated as follows:

$$\begin{aligned}
\frac{\partial L_x}{\partial x_i} &= \int_0^{t_{\max}} \boldsymbol{\lambda}_x{}^T \left[\frac{\partial \mathbf{M}}{\partial x_i}\ddot{\mathbf{u}} + \frac{\partial \mathbf{C}}{\partial x_i}\dot{\mathbf{u}} + \frac{\partial \mathbf{K}}{\partial x_i}\mathbf{u}\right] dt + \int_0^{t_{\max}} \left[\frac{1}{N_t}\tilde{\mathbf{F}}^T + \left(\ddot{\boldsymbol{\lambda}}_x\right)^T \mathbf{M} - \left(\dot{\boldsymbol{\lambda}}_x\right)^T \mathbf{C} + \left(\boldsymbol{\lambda}_x\right)^T \mathbf{K}\right]\frac{\partial \mathbf{u}}{\partial x_i} dt \\
&\quad + \left(\boldsymbol{\lambda}_x\big|_{t=t_{\max}}\right)^T \mathbf{M}\frac{\partial \mathbf{u}}{\partial x_i}\bigg|_{t=t_{\max}} + \left[\left(\boldsymbol{\lambda}_x\big|_{t=t_{\max}}\right)^T \mathbf{C} - \left(\dot{\boldsymbol{\lambda}}_x\big|_{t=t_{\max}}\right)^T \mathbf{M}\right]\frac{\partial \mathbf{u}}{\partial x_i}\bigg|_{t=t_{\max}}
\end{aligned} \tag{23}$$

Then, the adjoint conditions are obtained as:

$$\begin{cases}
\left(\ddot{\boldsymbol{\lambda}}_x(t)\right)^T \mathbf{M} - \left(\dot{\boldsymbol{\lambda}}_x(t)\right)^T \mathbf{C} + \left(\boldsymbol{\lambda}_x(t)\right)^T \mathbf{K} = -\frac{1}{N_t}\left(\tilde{\mathbf{F}}(t)\right)^T \\
\boldsymbol{\lambda}_x\big|_{t=t_{\max}} = \mathbf{0} \\
\dot{\boldsymbol{\lambda}}_x\big|_{t=t_{\max}} = \mathbf{0}
\end{cases} \tag{24}$$

Therefore, the sensitivity of L_x is determined by

$$\frac{\partial L_x}{\partial x_i} = \frac{\partial c}{\partial x_i} = \int_0^{t_{\max}} \boldsymbol{\lambda}_x{}^T \left[\frac{\partial \mathbf{M}}{\partial x_i}\ddot{\mathbf{u}} + \frac{\partial \mathbf{C}}{\partial x_i}\dot{\mathbf{u}} + \frac{\partial \mathbf{K}}{\partial x_i}\mathbf{u}\right] dt \tag{25}$$

When the loading amplitude of $\tilde{\mathbf{F}}(t)$ is considered as the stochastic variable, it is

converted to **Z** by using EOLE, and the sensitivity of dynamic compliance c w.r.t. **Z** is computed as below:

$$\frac{\partial c}{\partial Z_h}=\frac{\partial c}{\partial \tilde{F}_j}\frac{\partial \tilde{F}_j}{\partial Z_h}=\frac{\partial c}{\partial \tilde{F}_j}\frac{1}{\sqrt{\chi_h}}\mathbf{\Phi}_h(t)\rho_Y(t) \tag{26}$$

For computing $\frac{\partial c}{\partial \tilde{F}_j}$, a Lagrange equation L_f is constructed as

$$L_f=\frac{1}{N_t}\int_0^{t_{\max}}\tilde{\mathbf{F}}^T\mathbf{u}dt+\int_0^{t_{\max}}\boldsymbol{\lambda}_f{}^T\left[\mathbf{M}\ddot{\mathbf{u}}+\mathbf{C}\dot{\mathbf{u}}+\mathbf{K}\mathbf{u}-\tilde{\mathbf{F}}\right]dt \tag{27}$$

The sensitivity of L_f w.r.t. loading amplitude is as below:

$$\frac{\partial L_f}{\partial \tilde{F}_j}=\frac{1}{N_t}\int_0^{t_{\max}}\left[\mathbf{f}^T\mathbf{u}+\mathbf{Y}^T\frac{\partial \mathbf{u}}{\partial \tilde{F}_j}\right]dt+\int_0^{t_{\max}}\boldsymbol{\lambda}_f{}^T\left[\mathbf{M}\frac{\partial \ddot{\mathbf{u}}}{\partial \tilde{F}_j}+\mathbf{C}\frac{\partial \dot{\mathbf{u}}}{\partial \tilde{F}_j}+\mathbf{K}\frac{\partial \mathbf{u}}{\partial \tilde{F}_j}-\mathbf{f}\right]dt \tag{28}$$

where **f** represents $\frac{\partial \tilde{\mathbf{F}}}{\partial \tilde{F}_j}$. It is a vector composed of f_{lm}, in which l and m represent the l-th and m-th time instants. It satisfies the following conditions:

$$f_{lm}=\begin{cases}1 & l=m\\ 0 & l\neq m\end{cases} \tag{29}$$

Because there is no correlation between the initial conditions and loading amplitude, the finial term in Eq. (28) is transformed through integration by parts into

$$\begin{aligned}\frac{\partial L_f}{\partial \tilde{F}_j}=&\frac{1}{N_t}\int_0^{t_{\max}}\mathbf{f}^T\mathbf{u}dt-\int_0^{t_{\max}}\left(\boldsymbol{\lambda}_f\right)^T\mathbf{f}dt+\int_0^{t_{\max}}\left[\frac{1}{N}\tilde{\mathbf{F}}^T+\left(\ddot{\boldsymbol{\lambda}}_f\right)^T\mathbf{M}-\left(\dot{\boldsymbol{\lambda}}_f\right)^T\mathbf{C}+\left(\boldsymbol{\lambda}_f\right)^T\mathbf{K}\right]\frac{\partial \mathbf{u}}{\partial \tilde{F}_j}dt\\&+\left(\boldsymbol{\lambda}_f\Big|_{t=t_{\max}}\right)^T\mathbf{M}\frac{\partial \mathbf{u}}{\partial \tilde{F}_j}\Bigg|_{t=t_{\max}}+\left[\left(\boldsymbol{\lambda}_f\Big|_{t=t_{\max}}\right)^T\mathbf{C}-\left(\dot{\boldsymbol{\lambda}}_f\Big|_{t=t_{\max}}\right)^T\mathbf{M}\right]\frac{\partial \mathbf{u}}{\partial \tilde{F}_j}\Bigg|_{t=t_{\max}}\end{aligned} \tag{30}$$

Then, the adjoint conditions are obtained.

$$\begin{cases}\left(\ddot{\boldsymbol{\lambda}}_f(t)\right)^T\mathbf{M}-\left(\dot{\boldsymbol{\lambda}}_f(t)\right)^T\mathbf{C}+\left(\boldsymbol{\lambda}_f(t)\right)^T\mathbf{K}=-\frac{1}{N_t}\left(\tilde{\mathbf{F}}(t)\right)^T\\ \boldsymbol{\lambda}_f\Big|_{t=t_{\max}}=\mathbf{0}\\ \dot{\boldsymbol{\lambda}}_f\Big|_{t=t_{\max}}=\mathbf{0}\end{cases} \tag{31}$$

Therefore, the sensitivity of L_f is described as below:

$$\frac{\partial L_f}{\partial \tilde{F}_j}=\frac{\partial c}{\partial \tilde{F}_j}=\frac{1}{N_t}\int_0^{t_{\max}}\mathbf{f}^T\mathbf{u}dt-\int_0^{t_{\max}}\left(\boldsymbol{\lambda}_f\right)^T\mathbf{f}dt \tag{32}$$

The sensitivity of c w.r.t. Z_h is

$$\frac{\partial c}{\partial Z_h}=\frac{\partial c}{\partial \tilde{F}_j}\frac{\partial \tilde{F}_j}{\partial Z_h}=\left(\frac{1}{N_t}\int_0^{t_{\max}}\mathbf{f}^T\mathbf{u}dt-\int_0^{t_{\max}}\left(\boldsymbol{\lambda}_f\right)^T\mathbf{f}dt\right)\frac{1}{\sqrt{\chi_h}}\boldsymbol{\Phi}_h(t)\rho_Y(t) \tag{33}$$

Similarly, when the loading direction is treated as a stochastic variable, the Lagrange equation L_θ is constructed as follows:

$$L_\theta=\frac{1}{N_t}\int_0^{t_{\max}}\tilde{\mathbf{F}}^T\mathbf{u}dt+\int_0^{t_{\max}}\boldsymbol{\lambda}_\theta{}^T\left[\mathbf{M}\ddot{\mathbf{u}}+\mathbf{C}\dot{\mathbf{u}}+\mathbf{K}\mathbf{u}-\tilde{\mathbf{F}}\right]dt \tag{34}$$

Then, the sensitivity of L_θ w.r.t. loading direction is evaluated as follows:

$$\frac{\partial L_\theta}{\partial \theta}=\frac{\partial c}{\partial \theta}=\frac{1}{N_t}\int_0^{t_{\max}}\frac{\partial \tilde{\mathbf{F}}}{\partial \theta}^T\mathbf{u}dt-\int_0^{t_{\max}}\boldsymbol{\lambda}_\theta{}^T\frac{\partial \tilde{\mathbf{F}}}{\partial \theta}dt \tag{35}$$

The adjoint conditions are as follows:

$$\begin{cases}\left(\ddot{\boldsymbol{\lambda}}_\theta(t)\right)^T\mathbf{M}-\left(\dot{\boldsymbol{\lambda}}_\theta(t)\right)^T\mathbf{C}+\left(\boldsymbol{\lambda}_\theta(t)\right)^T\mathbf{K}=-\dfrac{1}{N_t}\left(\tilde{\mathbf{F}}(t)\right)^T\\ \dot{\boldsymbol{\lambda}}_\theta\big|_{t=t_{\max}}=\mathbf{0}\\ \boldsymbol{\lambda}_\theta\big|_{t=t_{\max}}=\mathbf{0}\end{cases} \tag{36}$$

3.4. Design sensitivity analysis

To tackle the TDRTO problem by using gradient-based optimization methods, the computation of design sensitivity is vital. Based on Eq. (10), the design sensitivity of objective function J w.r.t. ρ_e is as below:

$$\frac{\partial J}{\partial \rho_e}=\frac{\partial \mu}{\partial \rho_e}+\beta\frac{\partial \sigma}{\partial \rho_e} \tag{37}$$

To reduce the high computational cost of $\dfrac{\partial \mathbf{u}}{\partial \rho_e}$, a Lagrange function is constructed by incorporating an adjoint vector $\boldsymbol{\lambda}_\rho(t)$.

$$L_\rho=\frac{1}{N_t}\int_0^{t_{\max}}\tilde{\mathbf{F}}^T\mathbf{u}dt+\int_0^{t_{\max}}\boldsymbol{\lambda}_\rho{}^T\left[\mathbf{M}\ddot{\mathbf{u}}+\mathbf{C}\dot{\mathbf{u}}+\mathbf{K}\mathbf{u}-\tilde{\mathbf{F}}\right]dt \tag{38}$$

The sensitivity of L_ρ w.r.t. ρ_e is as below:

$$\frac{\partial L_\rho}{\partial \rho_e}=\frac{1}{N_t}\int_0^{t_{\max}}\tilde{\mathbf{F}}^T\frac{\partial \mathbf{u}}{\partial \rho_e}dt+\int_0^{t_{\max}}\boldsymbol{\lambda}_\rho{}^T\left[\frac{\partial \mathbf{M}}{\partial \rho_e}\ddot{\mathbf{u}}+\frac{\partial \mathbf{C}}{\partial \rho_e}\dot{\mathbf{u}}+\frac{\partial \mathbf{K}}{\partial \rho_e}\mathbf{u}\right]dt+\int_0^{t_{\max}}\boldsymbol{\lambda}_\rho{}^T\left[\mathbf{M}\frac{\partial \ddot{\mathbf{u}}}{\partial \rho_e}+\mathbf{C}\frac{\partial \dot{\mathbf{u}}}{\partial \rho_e}+\mathbf{K}\frac{\partial \mathbf{u}}{\partial \rho_e}\right]dt \quad (39)$$

Because there is no correlation between the initial conditions and design variables, the finial term in Eq. (39) is simplified as below:

$$\begin{aligned}&\int_0^{t_{\max}}\boldsymbol{\lambda}_\rho{}^T\left[\mathbf{M}\frac{\partial \ddot{\mathbf{u}}}{\partial \rho_e}+\mathbf{C}\frac{\partial \dot{\mathbf{u}}}{\partial \rho_e}+\mathbf{K}\frac{\partial \mathbf{u}}{\partial \rho_e}\right]dt\\&=\left(\boldsymbol{\lambda}_\rho\big|_{t=t_{\max}}\right)^T\mathbf{M}\frac{\partial \dot{\mathbf{u}}}{\partial \rho_e}\bigg|_{t=t_{\max}}-\left(\dot{\boldsymbol{\lambda}}_\rho\big|_{t=t_{\max}}\right)^T\mathbf{M}\frac{\partial \mathbf{u}}{\partial \rho_e}\bigg|_{t=t_{\max}}+\int_0^{t_{\max}}\left(\ddot{\boldsymbol{\lambda}}_\rho\right)^T\mathbf{M}\frac{\partial \mathbf{u}}{\partial \rho_e}dt\\&+\left(\boldsymbol{\lambda}_\rho\big|_{t=t_{\max}}\right)^T\mathbf{C}\frac{\partial \mathbf{u}}{\partial \rho_e}\bigg|_{t=t_{\max}}-\int_0^{t_{\max}}\left(\dot{\boldsymbol{\lambda}}_\rho\right)^T\mathbf{C}\frac{\partial \mathbf{u}}{\partial \rho_e}dt+\int_0^{t_{\max}}\left(\boldsymbol{\lambda}_\rho\right)^T\mathbf{K}\frac{\partial \mathbf{u}}{\partial \rho_e}dt\end{aligned} \quad (40)$$

Substituting Eq. (40) into Eq. (39), $\frac{\partial L_\rho}{\partial \rho_e}$ becomes

$$\begin{aligned}\frac{\partial L_\rho}{\partial \rho_e}&=\int_0^{t_{\max}}\boldsymbol{\lambda}_\rho{}^T\left[\frac{\partial \mathbf{M}}{\partial \rho_e}\ddot{\mathbf{u}}+\frac{\partial \mathbf{C}}{\partial \rho_e}\dot{\mathbf{u}}+\frac{\partial \mathbf{K}}{\partial \rho_e}\mathbf{u}\right]dt\\&+\int_0^{t_{\max}}\left[\frac{1}{N}\tilde{\mathbf{F}}^T+\left(\ddot{\boldsymbol{\lambda}}_\rho\right)^T\mathbf{M}-\left(\dot{\boldsymbol{\lambda}}_\rho\right)^T\mathbf{C}+\left(\lambda_\rho\right)^T\mathbf{K}\right]\frac{\partial \mathbf{u}}{\partial \rho_e}dt\\&+\left(\boldsymbol{\lambda}_\rho\big|_{t=t_{\max}}\right)^T\mathbf{M}\frac{\partial \dot{\mathbf{u}}}{\partial \rho_e}\bigg|_{t=t_{\max}}+\left[\left(\boldsymbol{\lambda}_\rho\big|_{t=t_{\max}}\right)^T\mathbf{C}-\left(\dot{\boldsymbol{\lambda}}_\rho\big|_{t=t_{\max}}\right)^T\mathbf{M}\right]\frac{\partial \mathbf{u}}{\partial \rho_e}\bigg|_{t=t_{\max}}\end{aligned} \quad (41)$$

Since Eq. (41) applies for any $\lambda_\rho(t)$, the adjoint vector is found by addressing the adjoint problem below:

$$\begin{cases}\left(\ddot{\boldsymbol{\lambda}}_\rho(t)\right)^T\mathbf{M}-\left(\dot{\boldsymbol{\lambda}}_\rho(t)\right)^T\mathbf{C}+\left(\boldsymbol{\lambda}_\rho(t)\right)^T\mathbf{K}=-\dfrac{1}{N_t}\tilde{\mathbf{F}}(t)^T\\ \boldsymbol{\lambda}_\rho\big|_{t=t_{\max}}=\mathbf{0}\\ \dot{\boldsymbol{\lambda}}_\rho\big|_{t=t_{\max}}=\mathbf{0}\end{cases} \quad (42)$$

Therefore, the sensitivity of L_ρ w.r.t. ρ_e is evaluated by

$$\frac{\partial L_\rho}{\partial \rho_e}=\frac{\partial c}{\partial \rho_e}=\frac{\partial \mu}{\partial \rho_e}=\int_0^{t_{\max}}\boldsymbol{\lambda}_\rho{}^T\left[\frac{\partial \mathbf{M}}{\partial \rho_e}\ddot{\mathbf{u}}+\frac{\partial \mathbf{C}}{\partial \rho_e}\dot{\mathbf{u}}+\frac{\partial \mathbf{K}}{\partial \rho_e}\mathbf{u}\right]dt \quad (43)$$

After computing the sensitivity of dynamic compliance w.r.t. ρ_e, the sensitivity of SD w.r.t. ρ_e is calculated by

$$\frac{\partial \sigma}{\partial \rho_e} = \frac{\sum_{i=1}^{n} 2 \frac{\partial c^2}{\partial x_i \partial \rho_e} \frac{\partial c}{\partial x_i} \sigma_{x_i}^2 + \sum_{j=1}^{m} 2 \frac{\partial c^2}{\partial Z_j \partial \rho_e} \frac{\partial c}{\partial Z_j} \sigma_{Z_j}^2}{2\sigma} \tag{44}$$

Therefore, it is necessary to solve $\frac{\partial c^2}{\partial x_i \partial \rho_e}$ and $\frac{\partial c^2}{\partial Z_j \partial \rho_e}$, where the Lagrange equation should be constructed twice.

For computing $\frac{\partial c^2}{\partial x_i \partial \rho_e}$, the Lagrange equation $L_{x\rho}$ is constructed as

$$L_{x\rho} = \int_0^{t_{\max}} \boldsymbol{\lambda}_x{}^T \left[\frac{\partial \mathbf{M}}{\partial x_i} \ddot{\mathbf{u}} + \frac{\partial \mathbf{C}}{\partial x_i} \dot{\mathbf{u}} + \frac{\partial \mathbf{K}}{\partial x_i} \mathbf{u} \right] dt + \int_0^{t_{\max}} \boldsymbol{\lambda}_{x\rho}{}^T \left[\mathbf{M}\ddot{\mathbf{u}} + \mathbf{C}\dot{\mathbf{u}} + \mathbf{K}\mathbf{u} - \tilde{\mathbf{F}} \right] dt \tag{45}$$

Then, the sensitivity of $L_{x\rho}$ w.r.t. ρ_e is as below:

$$\begin{aligned} \frac{\partial L_{x\rho}}{\partial \rho_e} = & \int_0^{t_{\max}} \boldsymbol{\lambda}_x{}^T \left[\frac{\partial \mathbf{M}^2}{\partial x_i \partial \rho_e} \ddot{\mathbf{u}} + \frac{\partial \mathbf{C}^2}{\partial x_i \partial \rho_e} \dot{\mathbf{u}} + \frac{\partial \mathbf{K}^2}{\partial x_i \partial \rho_e} \mathbf{u} \right] dt \\ & + \int_0^{t_{\max}} \boldsymbol{\lambda}_x{}^T \left[\frac{\partial \mathbf{M}}{\partial x_i} \frac{\partial \ddot{\mathbf{u}}}{\partial \rho_e} + \frac{\partial \mathbf{C}}{\partial x_i} \frac{\partial \dot{\mathbf{u}}}{\partial \rho_e} + \frac{\partial \mathbf{K}}{\partial x_i} \frac{\partial \mathbf{u}}{\partial \rho_e} \right] dt \\ & + \int_0^{t_{\max}} \boldsymbol{\lambda}_{x\rho}{}^T \left[\frac{\partial \mathbf{M}}{\partial \rho_e} \ddot{\mathbf{u}} + \frac{\partial \mathbf{C}}{\partial \rho_e} \dot{\mathbf{u}} + \frac{\partial \mathbf{K}}{\partial \rho_e} \mathbf{u} + \mathbf{M} \frac{\partial \ddot{\mathbf{u}}}{\partial \rho_e} + \mathbf{C} \frac{\partial \dot{\mathbf{u}}}{\partial \rho_e} + \mathbf{K} \frac{\partial \mathbf{u}}{\partial \rho_e} \right] dt \end{aligned} \tag{46}$$

Because there is no correlation between the initial conditions of structural properties and design variables, the finial term in the equation is transformed through integration by parts into

$$\begin{aligned} \frac{\partial L_{x\rho}}{\partial \rho_e} = & \int_0^{t_{\max}} \left[\boldsymbol{\lambda}_x{}^T \left(\frac{\partial \mathbf{M}^2}{\partial x_i \partial \rho_e} \ddot{\mathbf{u}} + \frac{\partial \mathbf{C}^2}{\partial x_i \partial \rho_e} \dot{\mathbf{u}} + \frac{\partial \mathbf{K}^2}{\partial x_i \partial \rho_e} \mathbf{u} \right) + \boldsymbol{\lambda}_{x\rho}{}^T \left(\frac{\partial \mathbf{M}}{\partial \rho_e} \ddot{\mathbf{u}} + \frac{\partial \mathbf{C}}{\partial \rho_e} \dot{\mathbf{u}} + \frac{\partial \mathbf{K}}{\partial \rho_e} \mathbf{u} \right) \right] dt \\ & + \int_0^{t_{\max}} \left[\left(\ddot{\boldsymbol{\lambda}}_x{}^T \frac{\partial \mathbf{M}}{\partial x_i} + \dot{\lambda}_{x\rho}{}^T \mathbf{M} \right) - \left(\dot{\boldsymbol{\lambda}}_x{}^T \frac{\partial \mathbf{C}}{\partial x_i} + \dot{\lambda}_{x\rho}{}^T \mathbf{C} \right) + \left(\boldsymbol{\lambda}_x{}^T \frac{\partial \mathbf{K}}{\partial x_i} + \boldsymbol{\lambda}_{x\rho}{}^T \mathbf{K} \right) \frac{\partial \mathbf{u}}{\partial \rho_e} \right] dt \\ & + \left[\left(\boldsymbol{\lambda}_x \big|_{t=t_{\max}} \right)^T \frac{\partial \mathbf{M}}{\partial x_i} + \left(\boldsymbol{\lambda}_{x\rho} \big|_{t=t_{\max}} \right)^T \mathbf{M} \right] \frac{\partial \dot{\mathbf{u}}}{\partial \rho_e} \Bigg|_{t=t_{\max}} \\ & + \left[\left(\left(\boldsymbol{\lambda}_x \big|_{t=t_{\max}} \right)^T \frac{\partial \mathbf{C}}{\partial x_i} + \left(\boldsymbol{\lambda}_{x\rho} \big|_{t=t_{\max}} \right)^T \mathbf{C} \right) - \left(\left(\dot{\boldsymbol{\lambda}}_x \big|_{t=t_{\max}} \right)^T \frac{\partial \mathbf{M}}{\partial x_i} + \left(\dot{\boldsymbol{\lambda}}_{x\rho} \big|_{t=t_{\max}} \right)^T \mathbf{M} \right) \right] \frac{\partial \mathbf{u}}{\partial \rho_e} \Bigg|_{t=t_{\max}} \end{aligned} \tag{47}$$

From the above, the adjoint equation is derived as

$$\begin{cases} \left(\ddot{\boldsymbol{\lambda}}_x{}^T \dfrac{\partial \mathbf{M}}{\partial x_i} + \dot{\boldsymbol{\lambda}}_{x\rho}{}^T \mathbf{M}\right) - \left(\dot{\boldsymbol{\lambda}}_x{}^T \dfrac{\partial \mathbf{C}}{\partial x_i} + \dot{\boldsymbol{\lambda}}_{x\rho}{}^T \mathbf{C}\right) + \left(\boldsymbol{\lambda}_x{}^T \dfrac{\partial \mathbf{K}}{\partial x_i} + \boldsymbol{\lambda}_{x\rho}{}^T \mathbf{K}\right) \dfrac{\partial \mathbf{u}}{\partial \rho_e} = 0 \\ \left(\boldsymbol{\lambda}_x\big|_{t=t_{\max}}\right)^T \dfrac{\partial \mathbf{M}}{\partial x_i} + \left(\boldsymbol{\lambda}_{x\rho}\big|_{t=t_{\max}}\right)^T \mathbf{M} = 0 \\ \left(\left(\boldsymbol{\lambda}_x\big|_{t=t_{\max}}\right)^T \dfrac{\partial \mathbf{C}}{\partial x_i} + \left(\boldsymbol{\lambda}_{x\rho}\big|_{t=t_{\max}}\right)^T \mathbf{C}\right) - \left(\left(\dot{\boldsymbol{\lambda}}_x\big|_{t=t_{\max}}\right)^T \dfrac{\partial \mathbf{M}}{\partial x_i} + \left(\dot{\boldsymbol{\lambda}}_{x\rho}\big|_{t=t_{\max}}\right)^T \mathbf{M}\right) = 0 \end{cases} \tag{48}$$

As shown in Eq. (24), since $\boldsymbol{\lambda}_x\big|_{t=t_{\max}} = 0$ and $\dot{\boldsymbol{\lambda}}_x\big|_{t=t_{\max}} = 0$, the Eq. (48) is simplified as below:

$$\begin{cases} \left(\ddot{\boldsymbol{\lambda}}_x{}^T \dfrac{\partial \mathbf{M}}{\partial x_i} + \dot{\boldsymbol{\lambda}}_{x\rho}{}^T \mathbf{M}\right) - \left(\dot{\boldsymbol{\lambda}}_x{}^T \dfrac{\partial \mathbf{C}}{\partial x_i} + \dot{\boldsymbol{\lambda}}_{x\rho}{}^T \mathbf{C}\right) + \left(\boldsymbol{\lambda}_x{}^T \dfrac{\partial \mathbf{K}}{\partial x_i} + \boldsymbol{\lambda}_{x\rho}{}^T \mathbf{K}\right) \dfrac{\partial \mathbf{u}}{\partial \rho_e} = 0 \\ \dot{\boldsymbol{\lambda}}_{x\rho}\big|_{t=t_{\max}} = \mathbf{0} \\ \boldsymbol{\lambda}_{x\rho}\big|_{t=t_{\max}} = \mathbf{0} \end{cases} \tag{49}$$

Then, the sensitivity of $L_{x\rho}$ w.r.t. ρ_e is expressed as

$$\begin{aligned} \frac{\partial L_{x\rho}}{\partial \rho_e} = \frac{\partial c^2}{\partial x_i \partial \rho_e} = &\int_0^{t_{\max}} \boldsymbol{\lambda}_x{}^T \left[\frac{\partial \mathbf{M}^2}{\partial x_i \partial \rho_e} \ddot{\mathbf{u}} + \frac{\partial \mathbf{C}^2}{\partial x_i \partial \rho_e} \dot{\mathbf{u}} + \frac{\partial \mathbf{K}^2}{\partial x_i \partial \rho_e} \mathbf{u}\right] dt \\ &+ \int_0^{t_{\max}} \boldsymbol{\lambda}_{x\rho}{}^T \left[\frac{\partial \mathbf{M}}{\partial \rho_e} \ddot{\mathbf{u}} + \frac{\partial \mathbf{C}}{\partial \rho_e} \dot{\mathbf{u}} + \frac{\partial \mathbf{K}}{\partial \rho_e} \mathbf{u}\right] dt \end{aligned} \tag{50}$$

For computing $\dfrac{\partial c^2}{\partial Z_h \partial \rho_e}$, differentiating Eq. (33) yields

$$\frac{\partial c^2}{\partial Z_h \partial \rho_e} = \frac{\partial c^2}{\partial \tilde{F}_j \partial \rho_e} \frac{\partial \tilde{F}_j}{\partial Z_h} + \frac{\partial L_f}{\partial \tilde{F}_j} \frac{\partial \tilde{F}_j{}^2}{\partial Z_h \partial \rho_e} \tag{51}$$

Since ρ_e and $\tilde{F}_j$ are independent, the last term in Eq. (51) equals zero. For the first term in Eq. (51), the Lagrange equation $L_{f\rho}$ is constructed as

$$L_{f\rho} = \frac{1}{N_t} \int_0^{t_{\max}} \mathbf{f}^T \mathbf{u} dt - \int_0^{t_{\max}} \left(\boldsymbol{\lambda}_f\right)^T \mathbf{f} dt + \int_0^{t_{\max}} \boldsymbol{\lambda}_{f\rho}{}^T \left[\mathbf{M}\ddot{\mathbf{u}} + \mathbf{C}\dot{\mathbf{u}} + \mathbf{K}\mathbf{u} - \tilde{\mathbf{F}}\right] dt \tag{52}$$

The sensitivity of $L_{f\rho}$ w.r.t. ρ_e is as follows:

$$\frac{\partial L_{f\rho}}{\partial \rho_e} = \frac{1}{N_t}\int_0^{t_{\max}} \mathbf{f}^T \frac{\partial \mathbf{u}}{\partial \rho_e} dt + \int_0^{t_{\max}} \boldsymbol{\lambda}_{f\rho}{}^T \left[\mathbf{M}\frac{\partial \ddot{\mathbf{u}}}{\partial \rho_e} + \mathbf{C}\frac{\partial \dot{\mathbf{u}}}{\partial \rho_e} + \mathbf{K}\frac{\partial \mathbf{u}}{\partial \rho_e} \right] dt + \int_0^{t_{\max}} \boldsymbol{\lambda}_{f\rho}{}^T \left[\frac{\partial \mathbf{M}}{\partial \rho_e}\ddot{\mathbf{u}} + \frac{\partial \mathbf{C}}{\partial \rho_e}\dot{\mathbf{u}} + \frac{\partial \mathbf{K}}{\partial \rho_e}\mathbf{u} \right] dt \tag{53}$$

Because there is no correlation between the initial conditions and loading amplitude and design variables, the finial term in Eq. (53) is transformed through integration by parts into

$$\begin{aligned} \frac{\partial L_{f\rho_e}}{\partial \rho_e} &= \int_0^{t_{\max}} \boldsymbol{\lambda}_{f\rho}{}^T \left[\frac{\partial \mathbf{M}}{\partial \rho_e}\ddot{\mathbf{u}} + \frac{\partial \mathbf{C}}{\partial \rho_e}\dot{\mathbf{u}} + \frac{\partial \mathbf{K}}{\partial \rho_e}\mathbf{u} \right] dt \\ &+ \int_0^{t_{\max}} \left[\frac{1}{N_t}\mathbf{f}^T + \left(\ddot{\boldsymbol{\lambda}}_{f\rho}\right)^T \mathbf{M} - \left(\dot{\boldsymbol{\lambda}}_{f\rho}\right)^T \mathbf{C} + \left(\boldsymbol{\lambda}_{f\rho}\right)^T \mathbf{K} \right] \frac{\partial \mathbf{u}}{\partial \rho_e} dt \\ &+ \left(\boldsymbol{\lambda}_{f\rho}\big|_{t=t_{\max}}\right)^T \mathbf{M} \frac{\partial \mathbf{u}}{\partial \rho_e}\bigg|_{t=t_{\max}} + \left[\left(\boldsymbol{\lambda}_{f\rho}\big|_{t=t_{\max}}\right)^T \mathbf{C} - \left(\dot{\boldsymbol{\lambda}}_{f\rho}\big|_{t=t_{\max}}\right)^T \mathbf{M} \right] \frac{\partial \mathbf{u}}{\partial \rho_e}\bigg|_{t=t_{\max}} \end{aligned} \tag{54}$$

From the above, the adjoint conditions are derived as

$$\begin{cases} \left(\ddot{\boldsymbol{\lambda}}_{f\rho}(t)\right)^T \mathbf{M} - \left(\dot{\boldsymbol{\lambda}}_{f\rho}(t)\right)^T \mathbf{C} + \left(\boldsymbol{\lambda}_{f\rho}(t)\right)^T \mathbf{K} = -\dfrac{1}{N_t}\mathbf{f}^T \\ \dot{\boldsymbol{\lambda}}_{f\rho}\big|_{t=t_{\max}} = \mathbf{0} \\ \boldsymbol{\lambda}_{f\rho}\big|_{t=t_{\max}} = \mathbf{0} \end{cases} \tag{55}$$

So, the sensitivity of $L_{f\rho}$ w.r.t. ρ_e is as follows:

$$\frac{\partial L_{f\rho_e}}{\partial \rho_e} = \frac{\partial c^2}{\partial \tilde{F}_j \partial \rho_e} = \int_0^{t_{\max}} \boldsymbol{\lambda}_{f\rho}{}^T \left[\frac{\partial \mathbf{M}}{\partial \rho_e}\ddot{\mathbf{u}} + \frac{\partial \mathbf{C}}{\partial \rho_e}\dot{\mathbf{u}} + \frac{\partial \mathbf{K}}{\partial \rho_e}\mathbf{u} \right] dt \tag{56}$$

And the sensitivity of $\dfrac{\partial c}{\partial Z_h}$ w.r.t. ρ_e is computed as

$$\frac{\partial c^2}{\partial Z_h \partial \rho_e} = \frac{\partial c^2}{\partial \tilde{F}_j \partial \rho_e}\frac{\partial \tilde{F}_j}{\partial Z_h} = \int_0^{t_{\max}} \boldsymbol{\lambda}_{f\rho}{}^T \left[\frac{\partial \mathbf{M}}{\partial \rho_e}\ddot{\mathbf{u}} + \frac{\partial \mathbf{C}}{\partial \rho_e}\dot{\mathbf{u}} + \frac{\partial \mathbf{K}}{\partial \rho_e}\mathbf{u} \right] dt \cdot \frac{1}{\sqrt{\chi_h}} \boldsymbol{\Phi}_h(t)\rho_Y(t) \tag{57}$$

For computing $\dfrac{\partial c^2}{\partial \theta \partial \rho_e}$, the Lagrange equation $L_{\theta\rho}$ is stated as follows:

$$L_{\theta\rho} = \frac{1}{N_t}\int_0^{t_{\max}} \frac{\partial \tilde{\mathbf{F}}}{\partial \theta}^T \mathbf{u} dt - \int_0^{t_{\max}} \boldsymbol{\lambda}_\theta{}^T \frac{\partial \tilde{\mathbf{F}}}{\partial \theta} dt + \int_0^{t_{\max}} \boldsymbol{\lambda}_{\theta\rho}{}^T [\mathbf{M}\ddot{\mathbf{u}} + \mathbf{C}\dot{\mathbf{u}} + \mathbf{K}\mathbf{u} - \tilde{\mathbf{F}}] dt \tag{58}$$

Therefore, the sensitivity of $L_{\theta\rho}$ w.r.t. ρ_e is as follows:

$$\frac{\partial L_{\theta\rho}}{\partial \rho_e}=\frac{\partial c^2}{\partial \theta \partial \rho_e}=\int_0^{t_{\max}} \boldsymbol{\lambda}_{\theta\rho}{}^T\left[\frac{\partial \mathbf{M}}{\partial \rho_e}\ddot{\mathbf{u}}+\frac{\partial \mathbf{C}}{\partial \rho_e}\dot{\mathbf{u}}+\frac{\partial \mathbf{K}}{\partial \rho_e}\mathbf{u}\right]dt \tag{59}$$

The adjoint equation is derived as

$$\begin{cases}\left(\ddot{\boldsymbol{\lambda}}_{\theta\rho}\right)^T\mathbf{M}-\left(\dot{\boldsymbol{\lambda}}_{\theta\rho}\right)^T\mathbf{C}+\left(\boldsymbol{\lambda}_{\theta\rho}\right)^T\mathbf{K}=-\dfrac{1}{N_t}\dfrac{\partial \tilde{\mathbf{F}}}{\partial \theta}^T \\ \dot{\boldsymbol{\lambda}}_{\theta\rho}\big|_{t=t_{\max}}=\mathbf{0} \\ \boldsymbol{\lambda}_{\theta\rho}\big|_{t=t_{\max}}=\mathbf{0}\end{cases} \tag{60}$$

Therefore, the sensitivities of SD w.r.t. ρ_e can be obtained by substituting Eqs. (25), (33), (35), (50), (57), and (59) into Eq. (44).

3.5. Numerical implementation

A pseudocode is illustrated to explain the computation process, as shown in Table 1. The moving asymptote algorithm (MMA) [57] is applied for updating design variables. Based on practical experience, parameter α = 0.05 is selected to ensure the accuracy and stability of the *HHT-α* method [58]. The density filter technique is applied to eliminate the checkerboard pattern [59], which transforms the design variables as follows:

$$\hat{x}_e=\frac{\sum_{l=1}^{NE}H_{e,l}x_l}{\sum_{l=1}^{NE}H_{e,l}} \tag{61}$$

where $\hat{x}$ denotes the modified design variables. $H_{e,l}=\max\left(0,r_{\min}-d\left(e,l\right)\right)$. $d(e,l)$ denotes the center distance. $r_{\min}$ represents the filtering radius.

Table 1 Pseudocode of TDRTO

Algorithm 1 Transient dynamic robust topology optimization
Input: design domain, design variables and uncertain parameters: structural properties, loading amplitude, loading directions, and maximum loading time $t_{\max}$.
Define *maxIter*, set *k*=0.
Initialize ϕ_e.
While $\delta < tol$ and *k*<*maxIter* **do**
iter= *iter* + 1.

Initialize the acceleration vector by solving the equation $\mathbf{M}\ddot{\mathbf{u}}_0 = (\mathbf{F}_0 - \mathbf{C}\dot{\mathbf{u}}_0 - \mathbf{K}\mathbf{u}_0)$.

for *i*=1: *N* **do**

Compute $\ddot{\mathbf{u}}_i$ using Eq. (18).

Update $\dot{\mathbf{u}}_i$ and $\mathbf{u}_i$ using Eq. (16).

end

Perform the sensitivity analysis using adjoint method. The sensitivities of stochastic and design variables are computed by Eqs. (43), (25), (33), and (35).

Compute the robust objective function using Eq. (10)and its sensitivities using Eq. (37).

Calculate the mean and variance using Eq. (14).

Perform the density filter using Eq. (61).

Update the design variables with MMA.

$\delta = \max\left(\phi_{new} - \phi_{old}\right)$.

end

4. Examples

This section presents three test examples, where the damping coefficients are denoted as $\alpha_r = 10$ and $\beta_r = 1\times10^{-5}$. For the 2D cases, the uncertainties of material property, loading direction, and time-variant loading magnitude are considered. For the 3D case, the uncertainties of geometric size, material property, loading direction, and time-variant loading amplitude are considered. To ensure stable convergence and clear topological structures, the penalty factor is fixed at 9 [59]. The minimum density filter radius $r_{\min}$ is 1.5 times the element length. All these codes are performed on the computer with configuration: Intel Core i9-10940X @3.4 GHz and 128GB RAM.

4.1. An L-shaped beam

An L-shaped beam is selected. The design domain is divided into 14,400 isoperimetric quadrilateral elements, as illustrated in Fig. 1. Its length *H* and width *L* o are 1 and 0.6 m, respectively. Stochastic variables, including material property, loading direction, and the loading amplitude, are assumed to follow a normal distribution. Their mean values, coefficients of variation (COVs), and SDs are shown in Table 2. The allowable volume fraction ratio is 50%. Three load cases, including $t_{\max}$ = 0.003, 0.005, and 0.1, are

considered.

Fig. 2 illustrates two different categories of stochastic loading amplitude. Both of them follow normal distributions and are generated by Monte Carlo simulation (MCS). The standard deviations of half-cycle sinusoidal loads are 100 and their means can be expressed as follows [58]:

$$F_{t_e} = F_0 \times \sin\left(\frac{\pi}{t_{\max}} \times t_e\right) \tag{62}$$

where t_e represents the *e*-th time instant. F_{t_e} represents the load amplitude at the *e*-th time instant. $t_{\max}$ represents the maximum loading time.

Fig. 2(a) demonstrates five half-cycle sinusoidal loads where time-variant stochasticity is not considered. In other words, the fluctuations of load amplitude only vary with the sine cycle and do not change over time. In contrast, the load amplitude in Fig. 2(b) considers time-variant stochasticity. The time-variant stochasticity is described by the autocorrelation function, which represents the correlation between different time points. The detailed description is as follows:

$$\rho_{\tilde{F}}\left(t_1, t_2\right) = \cos\left(\frac{10}{t_{\max}} \times \pi \times \left(t_2 - t_1\right)\right) \tag{63}$$

where t_1 and t_2 represent different time instants. $t_{\max}$ is the maximum loading time. The Gaussian process $\tilde{\mathbf{F}}(t)$ is decomposed by EOLE with 101 time nodes. For all methods, the maximum iteration is 400. The optimization cases are summarized as follows:

- Case 1: DTO;
- Case 2: RTO with COV=0.05 and β=1;
- Case 3: RTO with COV=0.05 and β=2;
- Case 4: RTO with COV=0.1 and β=1;
- Case 5: RTO with COV=0.1 and β=2;
- Case 6: TDRTO with COV=0.05 and β=1;
- Case 7: TDRTO with COV=0.05 and β=2;
- Case 8: TDRTO with COV=0.1 and β=1;

- Case 9: TDRTO with COV=0.1 and β=2.

Table 3 presents the optimal objective function values for DTO, RTO, and TDRTO, and Table 4 presents their optimal layouts. The convergence histories for RTO and TDRTO designs are presented in Fig. 3, and the validation results are obtained by MCS with 1×10^6 samples. The results are summarized in Table 5. J and J_{MCS} denote the objective function values and verification values of MCS, and ε represents the relative error. The conclusions are drawn as below:

(1) As shown in Table 3 and Table 4, the objective function values of Case 1 (DTO) are 0.0318, 0.0501, and 0.0346 for $t_{\max}$ = 0.003, 0.005, and 0.1, respectively. The results of Case 9 (TDRTO, COV=0.1, β=2) are 0.0383, 0.0607, and 0.0433 for $t_{\max}$ = 0.003, 0.005, and 0.1, respectively. Significant differences can be obtained between the optimal layouts of DTO and those of TDRTO, which highlight the importance of considering uncertain factors.

(2) Table 3 and Table 4 show that the TDRTO results considering time-variant characteristics are significantly different from those of RTO. For example, the objective function values of Case 5 (RTO, COV=0.1, β=2) are 0.0437, 0.0628, and 0.0498 for $t_{\max}$ = 0.1, 0.5, and 1, respectively, while the corresponding results of Case 9 (TDRTO, COV=0.1, β=2) results are 0.0383, 0.0607, and 0.0433. Additionally, Table 4 shows that the main structure of TDRTO is thicker than that of RTO, and the objective function is generally smaller. This indicates that TDRTO exhibits better structural stiffness than RTO, thereby improving the robustness.

(3) As shown in Table 3 and Table 4, the objective function values of Case 6 (TDRTO, COV=0.05, β=1) are 0.0335, 0.0538, and 0.0370 for $t_{\max}$ = 0.003, 0.005, and 0.1, respectively, while their values of Case 8 (TDRTO, COV=0.1, β=1) are 0.0351, 0.0578, and 0.0391. Under the same loading time, the structure demonstrates a certain degree of correlation. However, the perturbations caused by uncertainties increase with the increase of the COV, which amplifies the horizontal component of the load. To ensure the structural stability and mitigate the impact of these horizontal forces, additional horizontal elements are added to enhance the stiffness of the structure, thereby maximizing the robustness of the structure.

(4) Fig. 3 demonstrates that the objective function converges stably, where the iteration

curve is smooth after sufficient iterations. This verifies the good convergence of the TDRTO method. According to Table 5, it is apparent that all relative error indicators are smaller than 2%, which indicates the accuracy of the TDRTO method is acceptable.

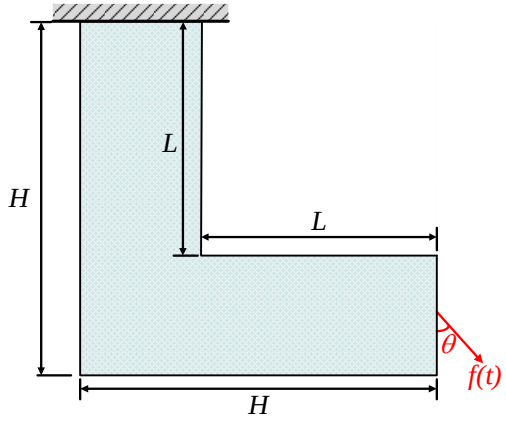

Fig. 1. Design domain of example 1.

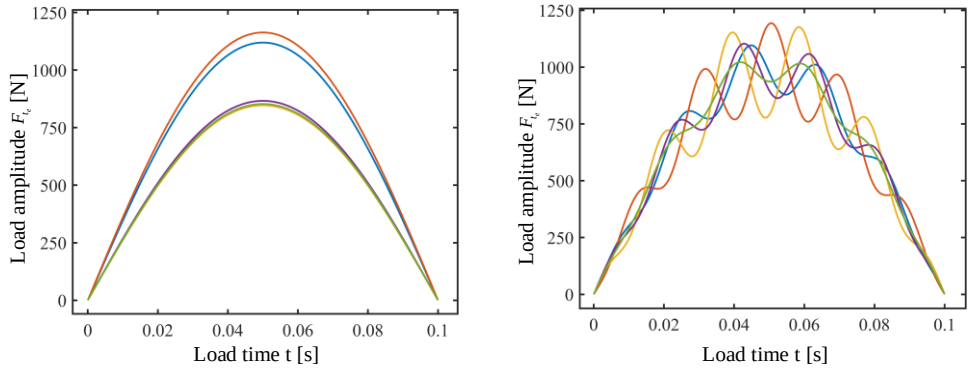

(a) loads without time-variant stochasticity (b) loads with time-variant stochasticity

Fig. 2. Half-cycle sinusoidal loading amplitude of two different cases for example 1.

Table 2. The means and SDs of stochastic variables for example 1.

Variables	E(GPa)	ρ (kg/ m^3)	F(KN)	θ (°)
Means	200	7800	1000	$\pi/12$
SDs (COV=5%)	10	390	50	$\pi/80$
SDs (COV=10%)	20	780	100	$\pi/40$

Table 3. Objective functions of $t_{\max}$ = 0.003, 0.005, and 0.1 for example 1.

Methods	Cases	Objective values ($\times 10^{-2}$)		
		$t_{\max}=0.003$	$t_{\max}=0.005$	$t_{\max}=0.1$
DTO	Case 1	3.178	5.005	3.459
RTO	Case 2	3.372	4.757	3.843
	Case 3	3.539	5.676	4.219

	Case 4	3.895	5.676	4.219
	Case 5	4.365	6.284	4.976
TDRTO	Case 6	3.348	5.382	3.696
	Case 7	3.507	5.781	3.914
	Case 8	3.507	5.781	3.914
	Case 9	3.827	6.065	4.332

Table 4. DTO, RTO, and TDRTO results of $t_{\max}$ = 0.003, 0.005, and 0.1 for example 1.

	$t_{\max} = 0.003$	$t_{\max} = 0.005$	$t_{\max} = 0.1$
Case 1	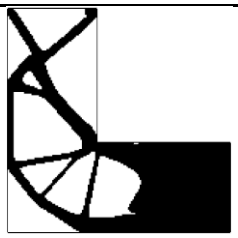	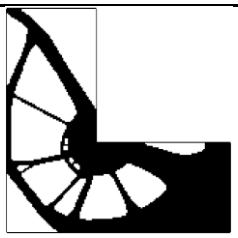	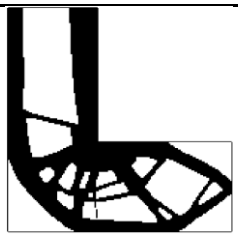
Case 2			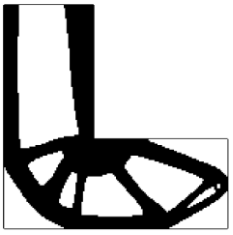
Case 3	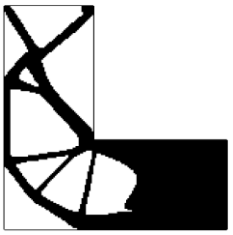		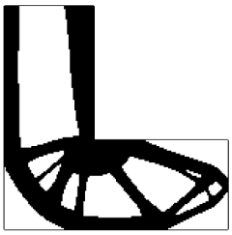
Case 4			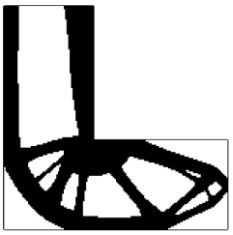
Case 5	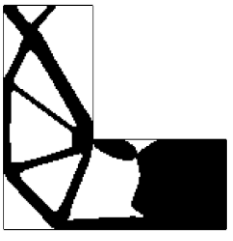		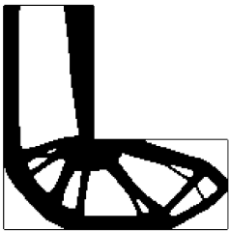

Case 6	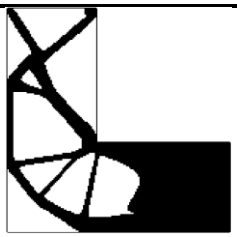	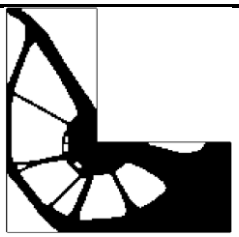	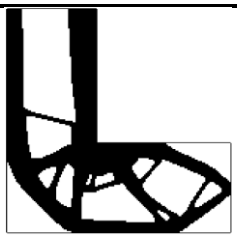
Case 7	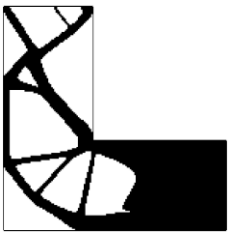		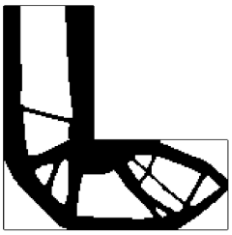
Case 8	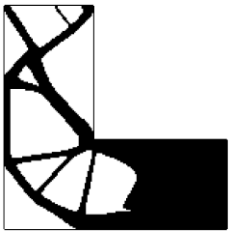		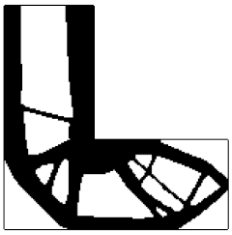
Case 9	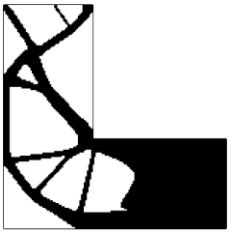	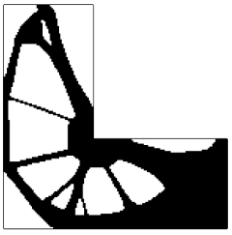	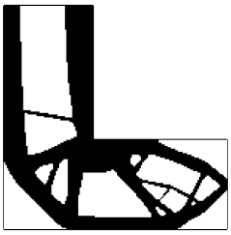

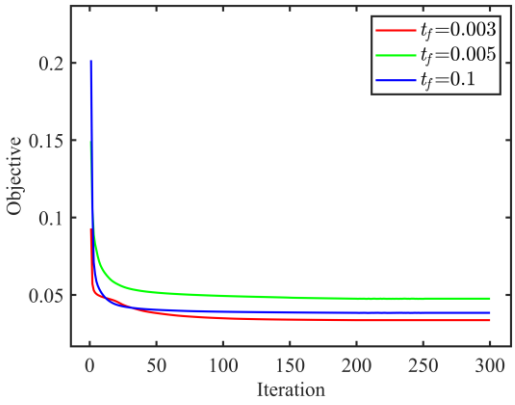

(a) RTO (COV=0.05, β=1)

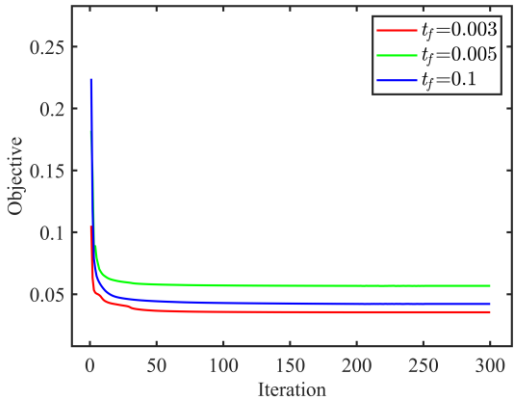

(b) RTO (COV=0.05, β=2)

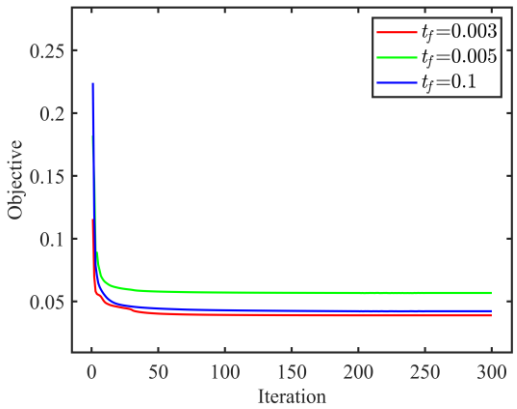

(c) RTO (COV=0.1, β =1)

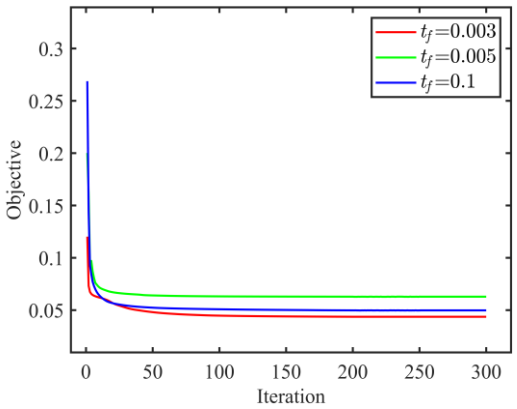

(d) RTO (COV=0.1, β =2)

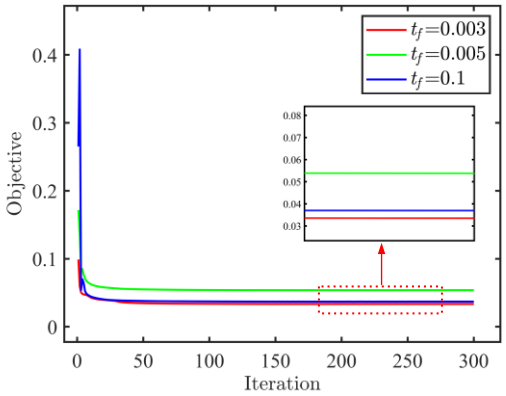

(e) TDRTO (COV=0.05, β =1)

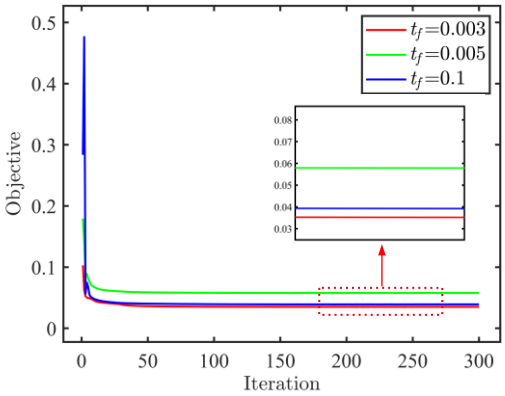

(f) TDRTO (COV=0.05, β =2)

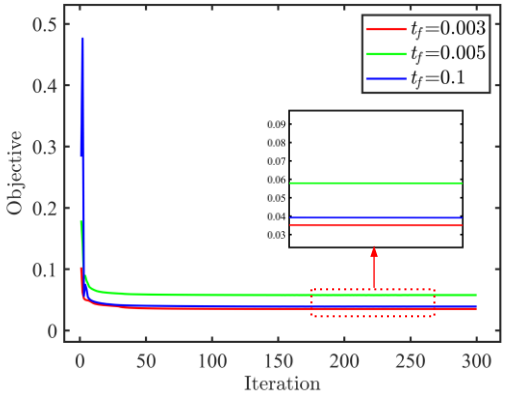

(g) TDRTO (COV=0.1, β =1)

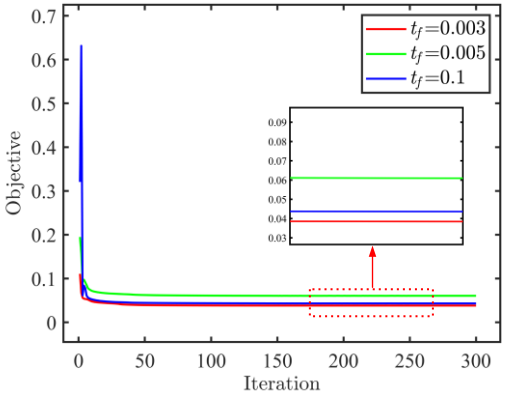

(h) TDRTO (COV=0.1, β =2)

Fig. 3. Convergence curves of RTO and TDRTO for example 1.

Table 5. Comparisons of different methods of $t_{\max}$ = 0.003, 0.005, and 0.1 for example 1.

Cases	Objective values ($\times 10^{-2}$)								
	$t_{\max}=0.003$			$t_{\max}=0.005$			$t_{\max}=0.1$		
	J	J_{MCS}	ε	J	J_{MCS}	ε	J	J_{MCS}	ε

Case 2	3.372	3.380	0.23%	4.757	4.702	1.17%	3.843	3.798	1.18%
Case 3	3.539	3.606	1.86%	5.676	5.699	0.40%	4.219	4.258	0.92%
Case 4	3.895	3.819	1.46%	5.676	5.641	0.62%	4.219	4.127	0.52%
Case 5	4.365	4.380	0.34%	6.284	6.315	0.49%	4.976	4.992	0.32%
Case 6	3.348	3.316	0.97%	5.382	5.373	0.17%	3.696	3.672	0.65%
Case 7	3.507	3.494	0.37%	5.781	5.755	0.45%	3.914	3.946	0.81%
Case 8	3.507	3.519	0.34%	5.781	5.763	0.31%	3.914	3.931	0.43%
Case 9	3.827	3.819	0.21%	6.065	6.090	0.41%	4.332	4.356	0.55%

4.2. A Clamped beam

A fixed beam experiences a half-cycle cosine force is applied at the midpoint of its lower span, as illustrated in Fig. 4. Its length L and width H are 12 and 2 m, respectively. The structure contains 15,606 elements. Stochastic variables are presented in Table 6. The allowable volume fraction ratio is 50%. Three load cases, i.e., $t_{\max}$ = 0.1, 0.5, and 1, are considered. Fig. 5 presents two types of loading amplitudes with $t_{\max}$ = 1, and both of them are generated by MCS. The standard deviations of five half-cycle cosine loads are 100 and their means are expressed as follows:

$$F_{t_e} = F_0 \times \cos\left(\frac{\pi}{t_{\max}} \times t_e\right) \tag{64}$$

Fig. 5(a) represents five half-cycle cosine loads without considering time-variant stochasticity, while Fig. 5(b) represents five half-cycle cosine loads with time-variant stochasticity. The autocorrelation function is as follows:

$$\rho_{\tilde{F}}\left(t_1, t_2\right) = \cos\left(\frac{10}{t_{\max}} \times \pi \times \left(t_2 - t_1\right)\right) \tag{65}$$

The stochastic process is discretized into 101 time nodes. The maximum iteration number is 400. The optimization cases are summarized as follows:

- Case 1: DTO;
- Case 2: RTO with COV=0.05 and β=1;
- Case 3: RTO with COV=0.05 and β=2;
- Case 4: RTO with COV=0.1 and β=1;
- Case 5: RTO with COV=0.1 and β=2;

- Case 6: TDRTO with COV=0.05 and β=1;

- Case 7: TDRTO with COV=0.05 and β=2;

- Case 8: TDRTO with COV=0.1 and β=1;

- Case 9: TDRTO with COV=0.1 and β=2.

Table 7 presents the optimal objective function values for DTO, RTO, and TDRTO. Table 8 presents their optimal layouts. The convergence histories for RTO and TDRTO design are shown in Fig. 6. The optima are validated by MCS with 1×10^6 samples, and the verification results are presented in Table 9.

As shown in Table 7 and Table 8, the objective function values of Case 1 (DTO) are 0.0088, 0.0086, and 0.0086 for $t_{\max}$ = 0.1, 0.5, and 1, respectively. The results of Case 8 (TDRTO, COV=0.1, β=1) are 0.0115, 0.0098, and 0.0096 for $t_{\max}$ = 0.1, 0.5, and 1, respectively. Significant differences are seen between the optimal layouts of DTO and TDRTO, which highlight the importance of considering uncertain factors. Additionally, the structural layout adaptively adjusts to ensure stability as the COV increases.

Table 7 and Table 8 show that the structures optimized by TDRTO have a more robust layout and smaller objective function values, which indicates that TDRTO achieves better structural stiffness than RTO. This emphasizes the importance of time-variant characteristics in enhancing structural robustness. Fig. 6 shows the iterative curve of the TDRTO method is stable. Furthermore, the relative error consistently remains below 2%, which shows the TDRTO method can provide enough accuracy, as demonstrated in Table 9.

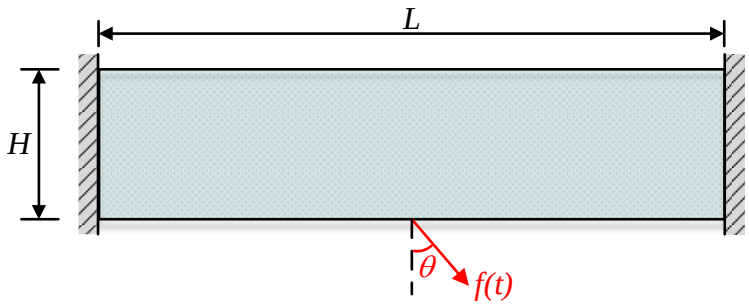

Fig. 4. Design domain of example 2.

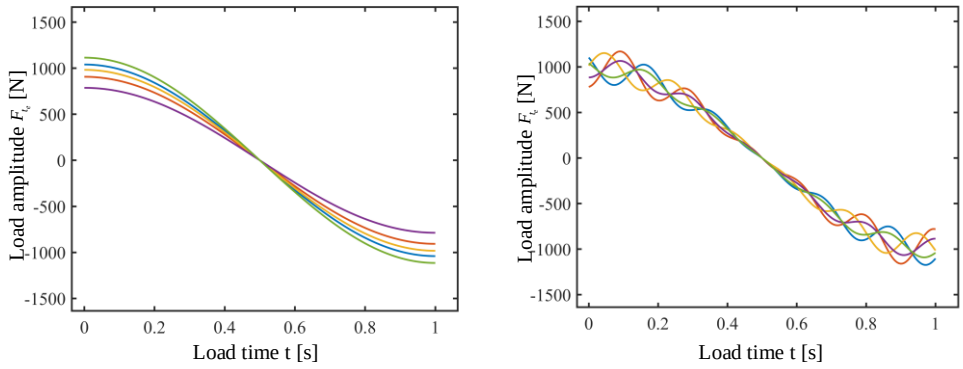

(a) loads without time-variant stochasticity (b) loads with time-variant stochasticity

Fig. 5. Half-cycle cosine loading amplitude of two different cases for example 2.

Table 6. The means and SDs of stochastic variables for example 2.

Variables	E(GPa)	ρ (kg/ m^3)	F(KN)	θ (°)
Means	200	7800	1000	$\pi/10$
SDs (COV=5%)	10	390	50	$\pi/50$
SDs (COV=10%)	20	780	100	$\pi/25$

Table 7. Objective functions of $t_{\max}$ = 0.1, 0.5, and 1 for example 2.

Methods	Cases	Objective values ($\times 10^{-2}$)		
		$t_{\max}=0.1$	$t_{\max}=0.5$	$t_{\max}=1$
DTO	Case 1	0.883	0.860	0.857
RTO	Case 2	1.089	0.949	0.945
	Case 3	1.106	1.040	1.041
	Case 4	1.106	1.040	1.041
	Case 5	1.321	1.246	1.231
TDRTO	Case 6	1.045	0.895	0.909
	Case 7	1.151	0.980	0.957
	Case 8	1.147	0.979	0.956
	Case 9	1.163	1.111	1.083

Table 8. DTO, RTO, and TDRTO results of $t_{\max}$ = 0.1, 0.5, and 1 for example 2.

	$t_{\max}=0.1$	$t_{\max}=0.5$	$t_{\max}=1$
Case 1			

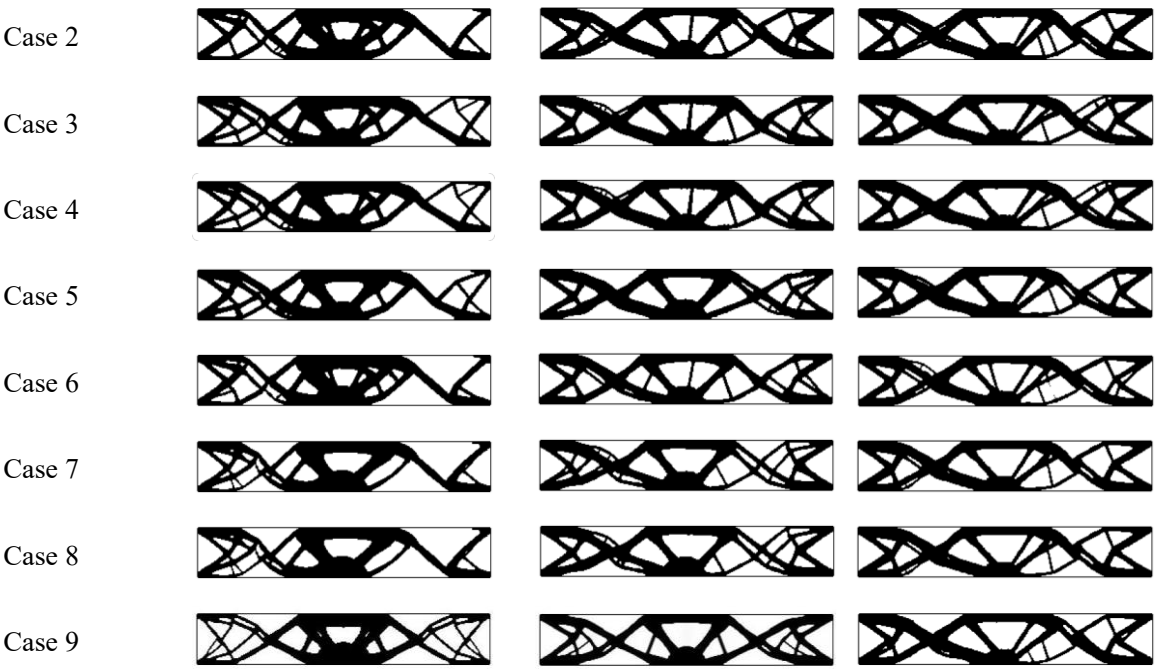

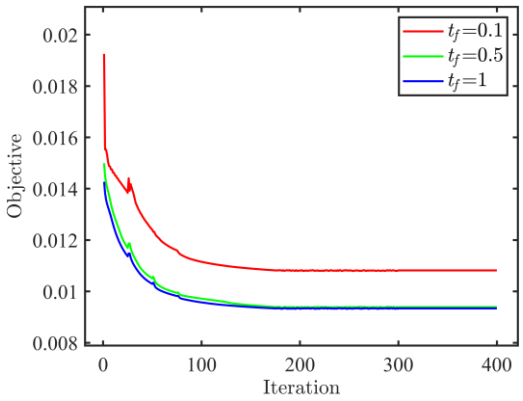

(a) RTO (COV=0.05, β=1)

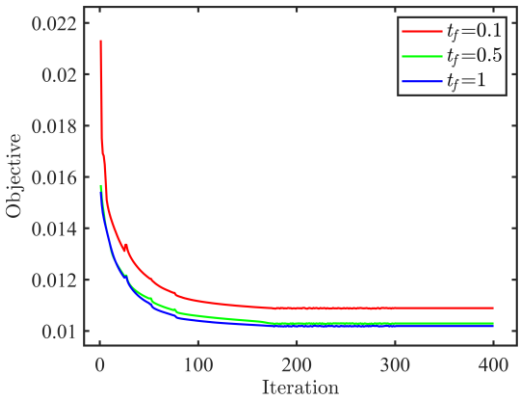

(b) RTO (COV=0.05, β=2)

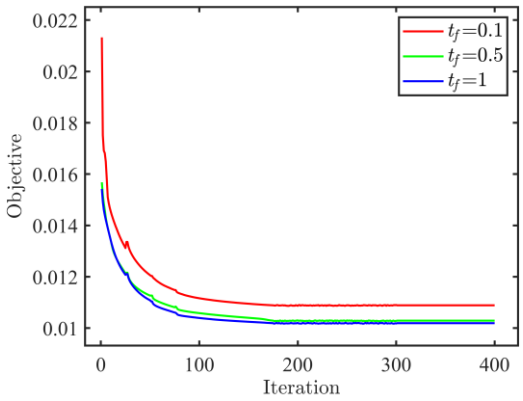

(c) RTO (COV=0.1, β=1)

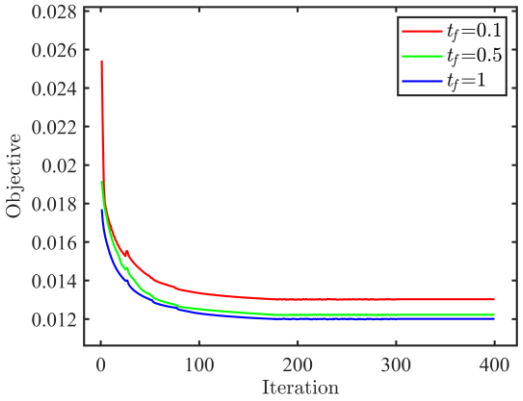

(d) RTO (COV=0.1, β=2)

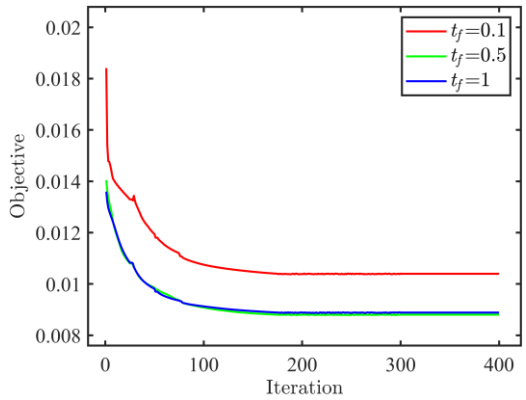

(e) TDRTO (COV=0.05, β=1)

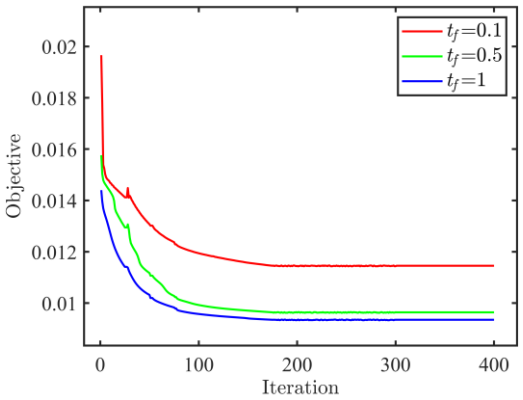

(f) TDRTO (COV=0.05, β=2)

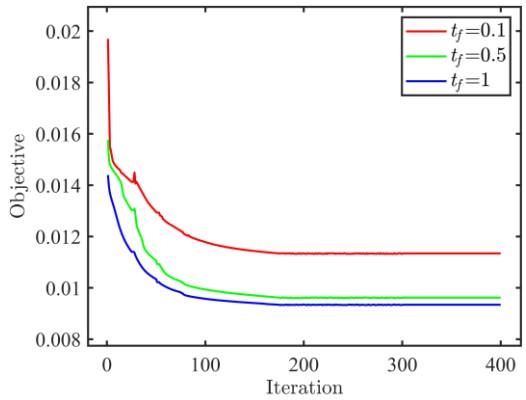

(g) TDRTO (COV=0.1, β=1)

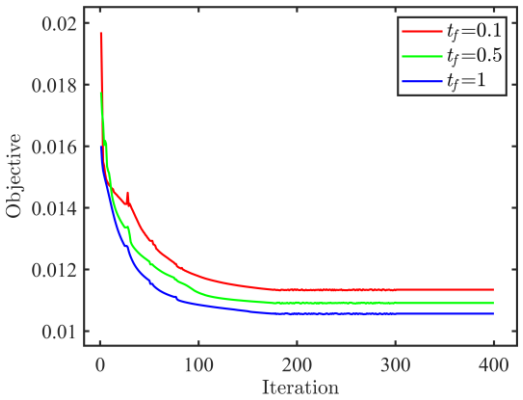

(h) TDRTO (COV=0.1, β=2)

Fig. 6. Convergence curves of RTO and TDRTO for example 2.

Table 9. Comparisons of different methods of $t_{\max}$ = 0.1, 0.5, and 1 for example 2.

Cases	Objective values ($\times 10^{-2}$)								
	$t_{\max}=0.1$			$t_{\max}=0.5$			$t_{\max}=1$		
	J	J_{MCS}	ε	J	J_{MCS}	ε	J	J_{MCS}	ε
Case 2	1.089	1.100	1.00%	0.949	0.936	1.39%	0.945	0.953	0.84%
Case 3	1.106	1.118	1.07%	1.040	1.052	1.14%	1.041	1.032	0.87%
Case 4	1.106	1.100	0.55%	1.040	1.031	0.87%	1.041	1.060	1.79%
Case 5	1.321	1.309	0.92%	1.246	1.257	0.88%	1.231	1.234	0.24%
Case 6	1.045	1.060	1.42%	0.895	0.899	0.44%	0.909	0.914	0.55%
Case 7	1.151	1.159	0.69%	0.980	0.992	1.21%	0.957	0.967	1.03%
Case 8	1.147	1.131	1.41%	0.979	0.963	1.66%	0.956	0.974	1.85%
Case 9	1.163	1.176	1.11%	1.111	1.125	1.24%	1.083	1.075	0.74%

4.3. A 3D cantilever beam

A typical 3D structure is optimized. The boundary conditions and design domain are

illustrated in Fig. 7(a). Four corners on the left end of the structure are fixed. A stochastic half-period sinusoidal load is exerted at the center of the right edge. The angle of the load is depicted in the Fig. 7(b). Its length *L*, width *D*, and thickness *H* are 320, 240, and 240 mm, respectively. The design domain is divided into $32\times24\times24$ 8-node isoperimetric hexahedral elements. The volume fraction ratio is limited to 40%. Two load cases, i.e. $t_{\max}$ = 0.1 and 1, are considered. Table 10 presents the means and SDs of stochastic variables, including geometric size, material property, loading amplitude, and loading direction. It should be noted that the description of vector forces in three-dimensional structures typically requires two angles, as shown in Fig. 7. By using the angle θ at the z-axis and the angle ξ at the x-axis, the force can be decomposed by

$$\begin{cases} F_x = F\sin\theta\cos\varsigma \\ F_y = F\sin\theta\sin\varsigma \\ F_z = F\cos\xi \end{cases} \tag{66}$$

Fig. 8 presents two types of loading amplitudes with $t_{\max}$ = 1, and they are generated by MCS. The standard deviations of five half-cycle cosine loads are 100 and their means are expressed as follows:

$$F_{t_e} = F_0 \times \sin\left(\frac{\pi}{t_{\max}} \times t_e\right) \tag{67}$$

Fig. 8(a) represents five half-cycle cosine loads without considering time-variant stochasticity, while Fig. 8(b) represents five half-cycle cosine loads with time-variant stochasticity. The autocorrelation function is as follows:

$$\rho_{\tilde{F}}\left(t_1,t_2\right) = \cos\left(\frac{10}{t_{\max}} \times \pi \times \left(t_2 - t_1\right)\right) \tag{68}$$

The stochastic process is discretized into 101 time nodes. The maximum iteration number is 180. The optimization cases are summarized as follows:

- Case 1: DTO;
- Case 2: RTO with COV=0.1 and β=1;
- Case 3: RTO with COV=0.1 and β=2;
- Case 4: RTO with COV=0.1 and β=4;
- Case 5: TDRTO with COV=0.1 and β=1;

- Case 6: TDRTO with COV=0.1 and β=2;

- Case 7: TDRTO with COV=0.1 and β=4;

Table 11 presents the optimal objective function values for DTO, RTO, and TDRTO, and Table 12 presents their optimal layouts. The convergence histories for RTO and TDRTO are shown in Fig. 9.

As shown in Table 11 and Table 12, it is evident that the optimal layouts of DTO and TDRTO show obvious differences, which highlight the importance of considering uncertain factors. As observed from Table 12, the objective function values of TDRTO, which accounts the time-variant characteristics, are significantly lower than those for RTO. These findings demonstrate that the consideration of time-variant characteristics contributes to maintain structural robustness. It also confirms the influence of uncertainty and time-variant characteristics on structural performance is obvious. Besides, the iterative curve in Fig. 9 demonstrates that the TDRTO method converges stably.

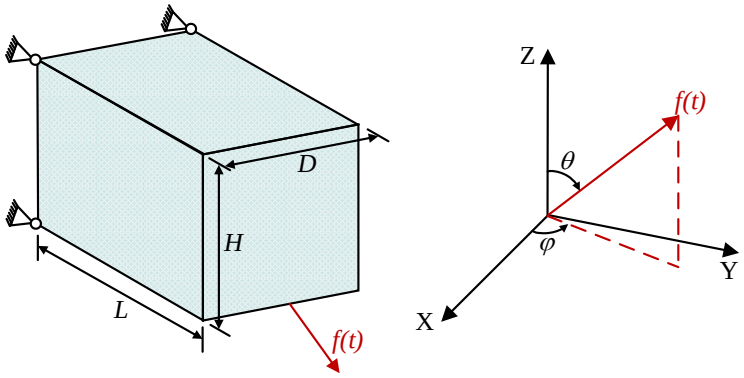

Fig. 7. The design problem of the 3D cantilever beam of example 3.

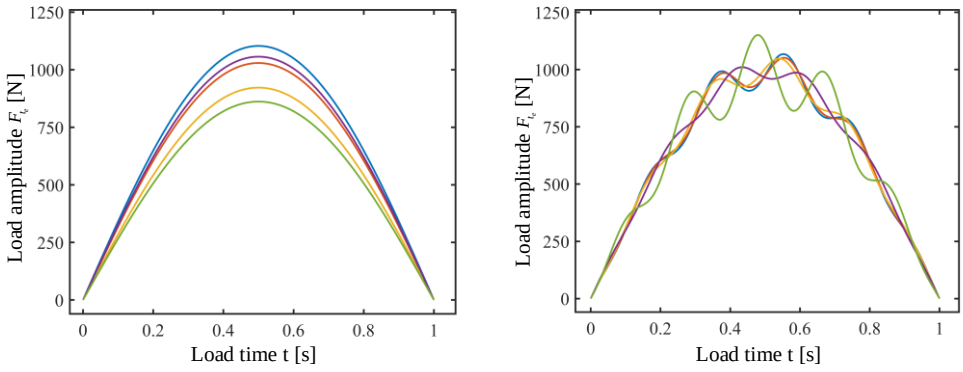

(a) loads without time-variant stochasticity (b) loads with time-variant stochasticity

Fig. 8. Loading amplitude of two different cases for example 3.

Table 10. The means and SDs of stochastic variables for example 3.

Variables	a(m)	b(m)	c(m)	E(GPa)	ρ (kg/ m^3)	F(KN)	θ (°)	φ (°)
Means	0.32	0.24	0.24	200	7800	1000	1.1π	0.5π
SDs	0.064	0.048	0.048	40	1560	200	$\pi/10$	$\pi/10$

Table 11. Results of optimization of $t_{\max}$ = 0.1 and 1 for example 3.

Methods	Cases	Objective values ($\times 10^{-2}$)	
		$t_{\max}=0.1$	$t_{\max}=1$
DTO	Case 1	0.268	0.467
RTO	Case 2	0.384	0.760
	Case 3	0.500	1.040
	Case 4	0.734	1.611
TDRTO	Case 5	0.320	0.688
	Case 6	0.372	0.906
	Case 7	0.473	1.342

Table 12. DTO and RTO results of $t_{\max}$ = 0.1 and 1 for example 3.

	$t_{\max}=0.1$	$t_{\max}=1$
Case 1	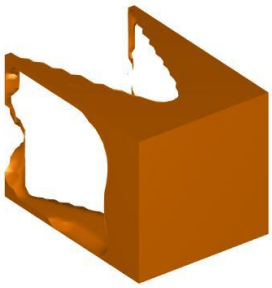	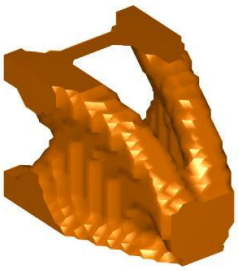
Case 2	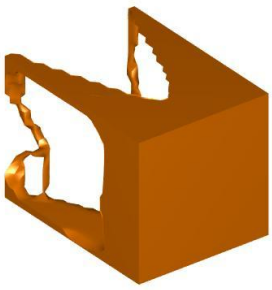	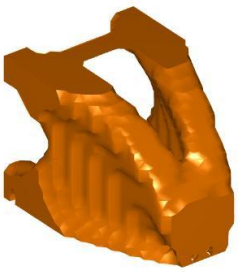

Case 3	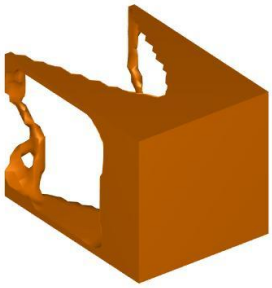	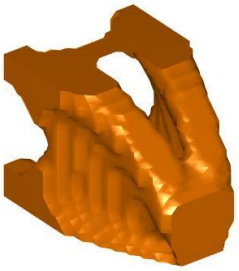
Case 4	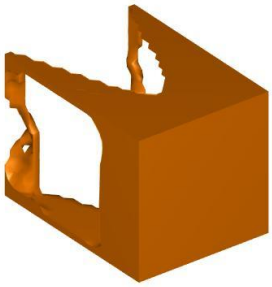	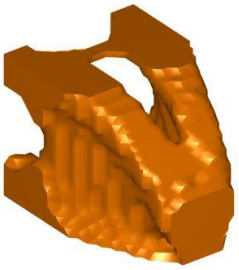
Case 5	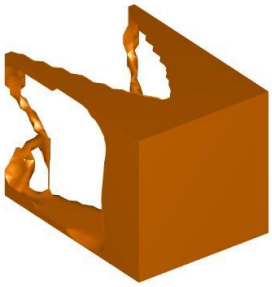	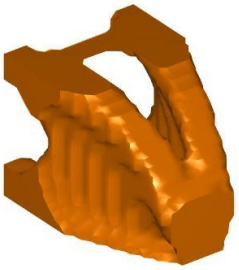
Case 6	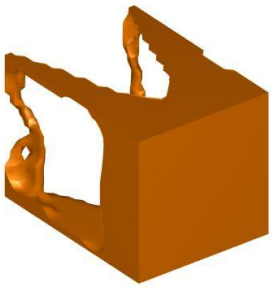	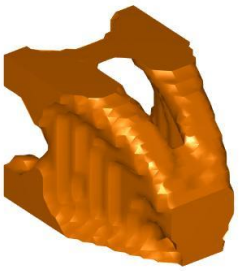
Case 7	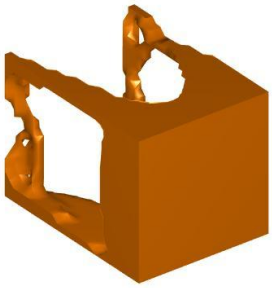	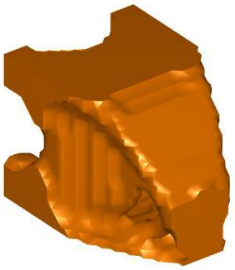

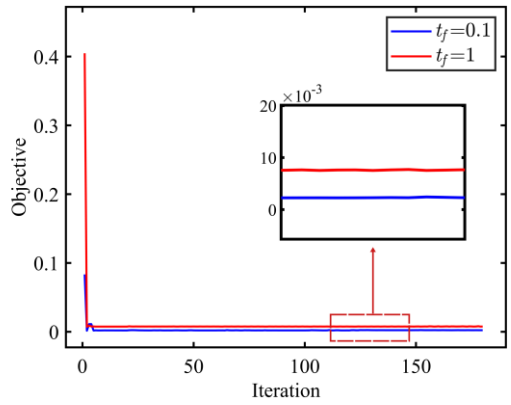

(a) COV=0.1, β =1

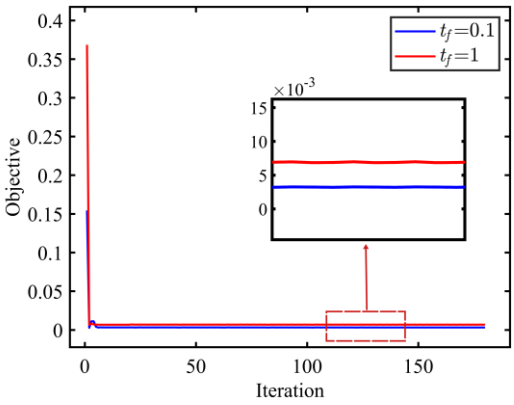

(d) TDRTO (COV=0.1, β =1)

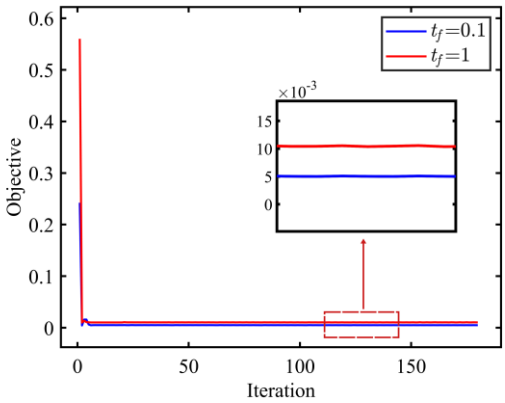

(b) COV=0.1, β =2

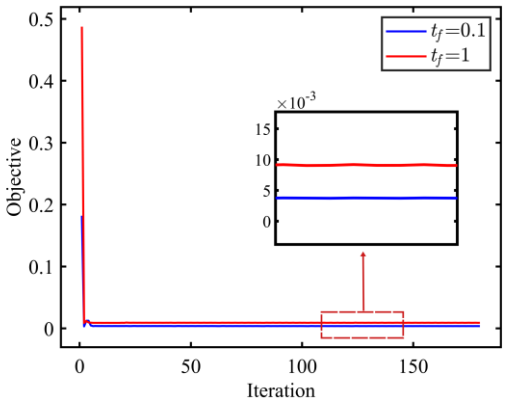

(e) TDRTO (COV=0.1, β =2)

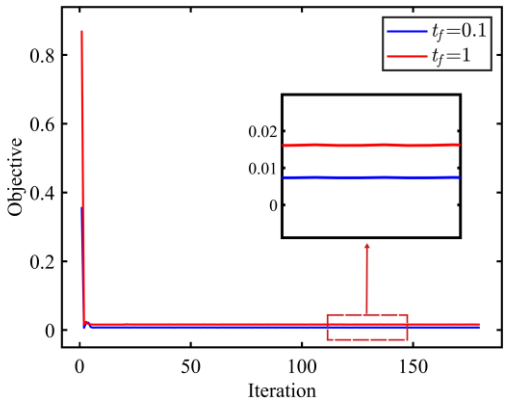

(c) COV=0.1, β =4

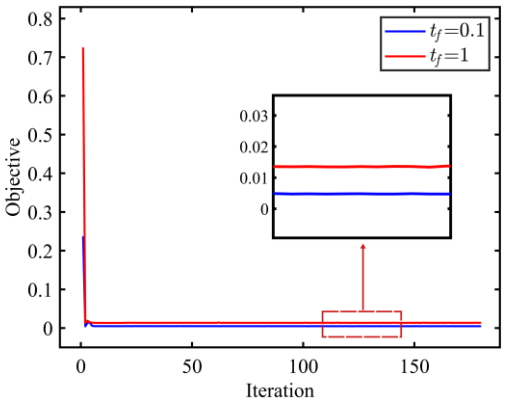

(f)TDRTO (COV=0.1, β =4)

Fig. 9. Convergence curves of RTO and TDRTO for example 3.

5. Conclusions

In this study, the TDRTO model is proposed to address transient dynamic RTO problems, which comprehensively considers the uncertainties in material parameters, loading direction, and time-variant loading amplitude. To discretize the time-variant loading amplitude, the

EOLE method is used, which can simulate the correlation of dynamic loads at different time instants. The design and stochastic sensitivities are derived by adjoint method and the "discretize-then-differentiate" approach, where the Lagrange equation is constructed twice. Besides, the *HHT-α* method is employed to address structural dynamic problems, thereby improving the computational efficiency.

Three numerical examples are examined to confirm the accuracy and efficiency of the TDRTO method by comparing its results with those of the RTO approach. The results show that time-variant uncertainties significantly impact the topology layout of structures, in which the structural layout tends to change for enhancing stiffness, thereby improving robustness. However, high-resolution large-scale computation remains a major challenge in dynamic topology optimization. In the future, some efficient frameworks or models, such as the second-order Arnoldi reduction approach [60] or dimensionality reduction methods [61], can be employed to decrease the computational cost for dynamic TO.

Acknowledgments

The supports of the National Natural Science Foundation of China (Grant Nos. 12372195), the Anhui Provincial Natural Science Foundation (Grant No. 2408085J007), the Dreams Foundation of Jianghuai Advance Technology Center (Grant NO. 2023-ZM01X013) are much appreciated.

Data availability

Data will be made available on request.

Reference

[1] M. Huang, C. Liu, Y. Guo, L. Zhang, Z. Du, X. Guo, A mechanics-based data-free Problem Independent Machine Learning (PIML) model for large-scale structural analysis and design optimization, Journal of the Mechanics and Physics of Solids, 193 (2024) 105893.

[2] H.A. Eschenauer, N. Olhoff, Topology optimization of continuum structures: a review, Appl. Mech. Rev., 54 (2001) 331-390.

[3] M.P. Bendsøe, N. Kikuchi, Generating optimal topologies in structural design using a homogenization method, Computer Methods in Applied Mechanics and Engineering 71 (1988) 197-224.

[4] P.K. Sahoo, S. Chatterjee, High-frequency vibrational control of principal parametric resonance of a nonlinear cantilever beam: Theory and experiment, Journal of Sound and Vibration 505 (2021) 116138.

[5] Y. Khulief, Dynamic response calculation of spatial elastic multibody systems with high-frequency excitation, Multibody System Dynamics 5 (2001) 55-78.
[6] X. Liang, J. Du, Concurrent multi-scale and multi-material topological optimization of vibro-acoustic structures, Computer Methods in Applied Mechanics and Engineering 349 (2019) 117-148.
[7] K. Zhou, Q.S. Li, Effects of time-variant modal frequencies of high-rise buildings on damping estimation, Earthquake Engineering & Structural Dynamics 50 (2021) 394-414.
[8] K. Zhang, N. Chen, J. Liu, M. Beer, A GRU-based ensemble learning method for time-variant uncertain structural response analysis, Computer Methods in Applied Mechanics and Engineering 391 (2022) 114516.
[9] B. Keshtegar, A. Farrokhian, R. Kolahchi, N.-T. Trung, Dynamic stability response of truncated nanocomposite conical shell with magnetostrictive face sheets utilizing higher order theory of sandwich panels, European Journal of Mechanics-A/Solids 82 (2020) 104010.
[10] Z.D. Ma, N. Kikuchi, I. Hagiwara, Structural topology and shape optimization for a frequency response problem, Computational Mechanics 13 (1993) 157-174.
[11] J. Pan, D.y. Wang, Topology optimization of truss structure with fundamental frequency and frequency domain dynamic response constraints, Acta Mechanica Solida Sinica 19 (2006) 231-240.
[12] G.H. Yoon, Structural topology optimization for frequency response problem using model reduction schemes, Computer Methods in Applied Mechanics and Engineering 199 (2010) 1744-1763.
[13] H. Liu, W. Zhang, T. Gao, A comparative study of dynamic analysis methods for structural topology optimization under harmonic force excitations, Structural and Multidisciplinary Optimization 51 (2015) 1321-1333.
[14] L. Shang, J. Zhai, Y. Miao, T. Tao, Improved mode acceleration-based vibroacoustic coupling analysis of functionally graded shell under random excitation, Applied Mathematical Modelling 109 (2022) 679-692.
[15] X. Liu, L. Gao, M. Xiao, An efficient multiscale topology optimization method for frequency response minimization of cellular composites, Engineering with Computers (2024) 1-25.
[16] S. Min, N. Kikuchi, Y. Park, S. Kim, S. Chang, Optimal topology design of structures under dynamic loads, Structural Optimization 17 (1999) 208-218.
[17] B. Kang, W. Choi, G. Park, Structural optimization under equivalent static loads transformed from dynamic loads based on displacement, Computers & Structures 79 (2001) 145-154.
[18] H.H. Jang, H.A. Lee, J. Lee, G.J. Park, Dynamic response topology optimization in the time domain using equivalent static loads, AIAA journal 50 (2012) 226-234.
[19] Y.I. Kim, G.J. Park, Nonlinear dynamic response structural optimization using equivalent static loads, Computer Methods in Applied Mechanics and Engineering 199 (2010) 660-676.
[20] M. Stolpe, On the equivalent static loads approach for dynamic response structural optimization, Structural and Multidisciplinary Optimization 50 (2014) 921-926.
[21] Y. Zhu, Z. Kang, An efficient transient dynamic topology optimization framework based on successive iteration of analysis and design, Computer Methods in Applied Mechanics and Engineering 421 (2024) 116787.

[22] Y. Wang, J. Gao, Z. Luo, T. Brown, N. Zhang, Level-set topology optimization for multimaterial and multifunctional mechanical metamaterials, Engineering Optimization 49 (2017) 22-42.
[23] E. Acar, G. Bayrak, Y. Jung, I. Lee, P. Ramu, S.S. Ravichandran, Modeling, analysis, and optimization under uncertainties: a review, Structural and Multidisciplinary Optimization 64 (2021) 2909-2945.
[24] Z. Meng, S. Lv, Y. Gao, C. Zhong, K. An, Data-driven reliability-based topology optimization by using the extended multi scale finite element method and neural network approach, Computer Methods in Applied Mechanics and Engineering, 438 (2025) 117837.
[25] K. Zhang, N. Chen, J. Liu, S. Yin, M. Beer, An efficient meta-model-based method for uncertainty propagation problems involving non-parameterized probability-boxes, Reliability Engineering & System Safety, 238 (2023) 109477.
[26] K. Zhang, N. Chen, P. Zeng, J. Liu, M. Beer, An efficient reliability analysis method for structures with hybrid time-dependent uncertainty, Reliability Engineering & System Safety, 228 (2022) 108794.
[27] T. Therneau, C. Crowson, E. Atkinson, Using time dependent covariates and time dependent coefficients in the cox model, Survival Vignettes, 2 (2017) 1-25.
[28] N. Changizi, G.P. Warn, Topology optimization of structural frames considering material nonlinearity and time-varying excitation, Structural and Multidisciplinary Optimization 63 (2021) 1789-1811.
[29] G.J. Park, Dynamic Response Optimization, Analytic Methods for Design Practice (2007) 255-308.
[30] L. Wang, Y. Ma, Y. Yang, X. Wang, Structural design optimization based on hybrid time-variant reliability measure under non-probabilistic convex uncertainties, Applied Mathematical Modelling 69 (2019) 330-354.
[31] S.A. Latifi Rostami, A. Kolahdooz, H. Chung, M. Shi, J. Zhang, Robust topology optimization of continuum structures with smooth boundaries using moving morphable components, Structural and Multidisciplinary Optimization, 66 (2023) 121.
[32] X. Guo, X. Zhao, W. Zhang, J. Yan, G. Sun, Multi-scale robust design and optimization considering load uncertainties, Computer Methods in Applied Mechanics and Engineering 283 (2015) 994-1009.
[33] J. Wu, J. Gao, Z. Luo, T. Brown, Robust topology optimization for structures under interval uncertainty, Advances in Engineering Software 99 (2016) 36-48.
[34] S.A.L. Rostami, M. Li, A. Kolahdooz, H. Chung, J. Zhang, Robust topology optimization of continuum structures under the hybrid uncertainties: a comparative study, Periodica Polytechnica Civil Engineering, 67 (2023) 637-645.
[35] S.A.L. Rostami, A. Kolahdooz, J. Zhang, Robust topology optimization under material and loading uncertainties using an evolutionary structural extended finite element method, Engineering Analysis with Boundary Elements, 133 (2021) 61-70.
[36] S.A.L. Rostami, A. Kolahdooz, J. Zhang, Robust topology optimization under material and loading uncertainties using an evolutionary structural extended finite element method, Engineering Analysis with Boundary Elements, 133 (2021) 61-70.
[37] X. Zhang, Z. Kang, W. Zhang, Robust topology optimization for dynamic compliance minimization under uncertain harmonic excitations with inhomogeneous eigenvalue analysis, Structural and Multidisciplinary Optimization 54 (2016) 1469-1484.
[38] J. Cai, L. Huang, H. Wu, L. Yin, Concurrent topology optimization of multiscale

structure under uncertain dynamic loads, International Journal of Mechanical Sciences 251 (2023) 108355.
[39] J. Zheng, Z. Luo, C. Jiang, J. Gao, Robust topology optimization for concurrent design of dynamic structures under hybrid uncertainties, Mechanical Systems and Signal Processing 120 (2019) 540-559.
[40] X.Y. Zhang, Z.H. Lu, S.Y. Wu, Y.G. Zhao, An efficient method for time-variant reliability including finite element analysis, Reliability Engineering & System Safety 210 (2021) 107534.
[41] L. Wang, X. Wang, X. Chen, R. Wang, Time-variant reliability model and its measure index of structures based on a non-probabilistic interval process, Acta Mechanica 226 (2015) 3221-3241.
[42] P. Venini, Dynamic compliance optimization: Time vs frequency domain strategies, Computers & Structures, 177 (2016) 12-22.
[43] H. Zhang, X. Ding, W. Ni, Y. Chen, X. Zhang, H. Li, Concurrent topology optimization of composite plates for minimum dynamic compliance, Materials, 15 (2022) 538.
[44] G. Allaire, C. Dapogny, F. Jouve, Shape and topology optimization, Handbook of numerical analysis, Elsevier, 2021, pp. 1-132.
[45] M. Stolpe, K. Svanberg, An alternative interpolation scheme for minimum compliance topology optimization, Structural and Multidisciplinary Optimization 22 (2001) 116-124.
[46] F. Wang, B.S. Lazarov, O. Sigmund, On projection methods, convergence and robust formulations in topology optimization, Structural and Multidisciplinary Optimization 43 (2011) 767-784.
[47] M.P. Bendsoe, O. Sigmund, Topology optimization: theory, methods, and applications, Springer Science & Business Media, 2013.
[48] Z. Meng, Y. Wu, X. Wang, S. Ren, B. Yu, Robust topology optimization methodology for continuum structures under probabilistic and fuzzy uncertainties, International Journal for Numerical Methods in Engineering 122 (2021) 2095-2111.
[49] M. Habashneh, M.M. Rad, Reliability based topology optimization of thermoelastic structures using bi-directional evolutionary structural optimization method, International Journal of Mechanics and Materials in Design 19 (2023) 605-620.
[50] L. Bruno, C. Canuto, D. Fransos, Stochastic aerodynamics and aeroelasticity of a flat plate via generalised polynomial chaos, Journal of Fluids and Structures 25 (2009) 1158-1176.
[51] Y. Wu, E. Li, Z. He, X. Lin, H. Jiang, Robust concurrent topology optimization of structure and its composite material considering uncertainty with imprecise probability, Computer Methods in Applied Mechanics and Engineering 364 (2020) 112927.
[52] H.G. Beyer, B. Sendhoff, Robust optimization–a comprehensive survey, Computer Methods in Applied Mechanics and Engineering 196 (2007) 3190-3218.
[53] N. Gan, Q. Wang, Topology optimization design of improved response surface method for time-variant reliability, Advances in Engineering Software 146 (2020) 102828.
[54] C.C. Li, A. Der Kiureghian, Optimal discretization of random fields, Journal of Engineering Mechanics 119 (1993) 1136-1154.
[55] H.M. Hilber, T.J. Hughes, R.L. Taylor, Improved numerical dissipation for time integration algorithms in structural dynamics, Earthquake Engineering & Structural Dynamics 5 (1977) 283-292.
[56] J. Chung, G.M. Hulbert, A Time Integration Algorithm for Structural Dynamics With

Improved Numerical Dissipation: The Generalized-α Method, Journal of Applied Mechanics 60 (1993) 371-375.
[57] N.M. Newmark, A method of computation for structural dynamics, Journal of the Engineering Mechanics Division 85 (1959) 67-94.
[58] K. Svanberg, The method of moving asymptotes—a new method for structural optimization, International Journal for Numerical Methods in Engineering 24 (1987) 359-373.
[59] Giraldo-Londoño, G.H. Paulino, PolyDyna: a Matlab implementation for topology optimization of structures subjected to dynamic loads, Structural and Multidisciplinary Optimization 64 (2021) 957-990.
[60] K.-I. Ypsilantis, G. Kazakis, M.G. Faes, J. Ivens, N.D. Lagaros, D. Moens, A topology-based in-plane filtering technique for the combined topology and discrete fiber orientation optimization, Computer Methods in Applied Mechanics and Engineering 417 (2023) 116400.
[61] K. Long, X. Yang, N. Saeed, R. Tian, P. Wen, X. Wang, Topology optimization of transient problem with maximum dynamic response constraint using SOAR scheme, Frontiers of Mechanical Engineering 16 (2021) 593-606.
[62] M. Xiao, J. Ma, X. Gao, P. Breitkopf, B. Raghavan, W. Zhang, L. Cauvin, P. Villon, Primal–dual on-the-fly reduced-order modeling for large-scale transient dynamic topology optimization, Computer Methods in Applied Mechanics and Engineering 428 (2024) 117099.